A NOVEL BEAM STEERABLE ANTENNA ARRAY SYSTEM FOR 5G MM-WAVE APPLICATIONS

by
AMIR MOHSEN AHMADI NAJAFABADI

Submitted to the Graduate School of Engineering and Natural Sciences
in partial fulfilment of
the requirements for the degree of Master of Science

Sabancı University
June 2022

ABSTRACT

A NOVEL BEAM STEERABLE ANTENNA ARRAY SYSTEM FOR 5G MM-WAVE APPLICATIONS

AMIR MOHSEN AHMADI NAJAFABADI

Electronics Engineering M.Sc Thesis, June 2022

Thesis Supervisor: Prof. Ibrahim Tekin

Keywords: Beam Steering, Multibeam Array Antennas, Beam Forming Network, Fifth-Generation (5G) Antennas, Millimeter-Waves, Microstrip Arrays, Series-Fed Arrays, Wide-Band Antennas, 28 GHz.

This thesis proposes a novel, low-cost, wide-angle beam steerable microstrip antenna array system for 5G 28 GHz mm-wave band applications. The final system consists of two branch-line couplers on the perpendicular sides and one butler matrix on the main side of the final structure, together with their corresponding Chebyshev tapered antenna arrays. Unlike the conventional 4×4 Butler matrix and branch-line coupler feeding, which generally can generate 4 and 2 beams, the designed configuration employs a novel feeding technique that allows the system to generate 7 beams for the butler matrix and 3 beams for the branch-line coupler. The final system covers a wider spatial range due to its unique placement of the branch-line couplers and 2×10 array antennas perpendicular to the sides of the main beamforming and the 4×10 array antenna architecture. The measured gain for the 13 beams varied between 11.2 and 14.1 dBi at 28 GHz. A wide impedance bandwidth for the entire 26.5 to 29.5 GHz band was achieved, while more than a 10% fractional radiation bandwidth was obtained with a gain value over 10 dBi. Furthermore, to enhance the radiation bandwidth of the system, a novel slot-loaded unit element is designed and optimized for the corresponding beamforming network to operate at the band of interest. The proposed design's overall performance was verified, and a low-cost PCB prototyping technique was used for fabricating. Later the fabricated design's reflection coefficients and radiation patterns were measured. The final system's low-cost, wide beam coverage and improved realized gain values make it suitable for 5G mm-wave handset applications.

ÖZET

5G MİLİMETRE DALGA UYGULAMALARI İÇİN ÖZGÜN BİR IŞIN HUZMESİ YÖNLENDİRİLEBİLEN ANTEN DİZİN SİSTEMİ

AMIR MOHSEN AHMADI NAJAFABADI

Yüksek Lisans Tezi, HAZİRAN 2022

Tez Danışmanı: Prof. Dr. Ibrahim Tekin

Anahtar Kelimeler: Işın Huzmesi Yönlendirilebilen, Çoklu Huzmeli Anten Dizinleri, Işın Huzmesi Şekillendirme Ağları, 5G Antenleri, Milimetre Dalga, Mikroeşit Dizinleri, Seri-Beslenme Dizinleri, Geniş-Bantlı Antenler, 28 GHz

Bu tezde 5G 28 GHz milimetre (mm) dalga uygulamaları için özgün, düşük maliyetli, geniş açılı ve ışın huzmesi yönlendirebilen bir mikroşerit anten dizin sistemi önerilmiştir. Son sistem dikey olarak yanlara yerleştirilmiş iki kol hattı kuplaj ve ana yüzeye yerleştirilmiş bir Butler matrisi ve onlara bağlanmış $N \times 10$ anten dizinlerinden ibarettir. Sırasıyla, 4 ve 2 ışın üretebilen geleneksel 4×4 Butler matrisi ve kol hattı kuplaj elemanından farklı olarak, bu tasarımda, özgün bir besleme tekniği kullanılmaktadır. Bu sayede, sistem Butler matrisi için 7 ışın ve kol hattı kuplaj elemanı için 3 ışın üretebilmiştir. Sistemin en son konumlandırmasında, kol hattı kuplaj elemanı ana huzme şekillendirme ve 4×10 dizinine dikey bir şekilde yerleştirilerek sistemin daha geniş bir açısal kapsama sahip olması sağlanmıştır. 13 ışın için ölçülen kazanç seviyesi 28 GHz'de 11.2 ile 14.1 dBi seviyeleri arasındadır. Bu sistem sayesinde 26.5 ve 29.5 GHz bandının tamamını kapsayacak geniş bir empedans bant genişliği elde edilmiştir, ayrıca kazanç değerinin 10 dBi üzerinde olduğu %10 bir fraksiyonel yayılım bant genişliği sağlanmıştır. Ayrıca, yayılım bant genişliğinin iyileştirilmesi için belirtilen bantta özgün bir yarık anten dizini tasarlanmıştır. Tasarımın doğrulanabilmesi için düşük maliyetli PCB prototipleme tekniği kullanılmıştır ve üretimden sonra tasarımın yansıma katsayıları ve yayılım örüntülerinin ölçümleri yapılmıştır. Düşük maliyeti, geniş açısal kapsamı ve yükseltilmiş kazancı bu sistemi 5G mm-dalga el aygıtları uygulamalarında kullanılması için uygun bir aday haline getirmiştir.

ACKNOWLEDGEMENTS

First, I would like to convey my deep appreciation to my advisor, Prof. Ibrahim Tekin, for his continuous support, patience, and guidance during my graduate studies at Sabanci University. It would not be possible for me to move forward without his help and motivation. He supports me throughout my studies in various manners, both academically and personally. It was a great pleasure to work with Prof. Ibrahim Tekin, and surely his encouragement and helps will continue to motivate me even after my studies at Sabanci University.

I also would like to express my special thanks to Prof. Husnu Yenigun. It is impossible to explain my gratitude to Prof. Yengiun for his support and kindness.

I also would like to share my highest gratitude to Prof. Sema Dumanli Oktar. She was the one who initiated my devotion to this field with her enthusiasm and continuously has been supported me during these years.

I also would like to thank Prof. Vakur Erturk, who started for me the joy of learning and teaching electromagnetic during my undergraduate years and supported and guided me on this path.

I want to thank my colleague in RF/Wireless lab, Firas Abdul Ghani, my friends at Sabanci University, Ammar Saleem, Esaam Jamil, Saeed Nourizadeh, Hayrettin Ayar, Mikail Erdem, Isa Ugurlu. I want to thank our technicians, Ali Kasal, Sercan Tanyeli, and Baris Tumer, for their support.

Lastly, I want to thank my father for all he did for me, he was more than a father to me, and I cannot ever repay all the goods he did for me.

Finally, I would like to express my greatest appreciation to my thesis jury members for their valuable time and consideration.

Additionally, I would like to acknowledge that this work was supported in part by the Scientific and Technological Research Council of Turkey (TUBITAK), Grant No: 118E842.

To the tyranny of the merit

Table of Contents

List of Tables

List of Figures

List of Abbreviations

3GPP The 3rd Generation Partnership Project.

4G Fourth-generation.

5G Fifth-generation.

BB Baseband.

BFN Beamforming Network.

BLC Branch Line Coupler.

BM Butler Matrix.

Gbps Gigabits per second.

IF Intermediate Frequency.

IL Insertion Loss.

MIOT Massive Internet of Things.

mm-wave Millimeter Wave.

PAA Phased Array Antennas.

PGTL Phase Gradient Transmission Line.

RF Radio Frequency.

RTPS Reflective Loads Phase Shifter.

SIW Substrate Integrated Waveguide.

SLL Side Lobe Level.

SP4T Single-pole Four Throws.

VNA Vector Network Analyzer.

Chapter 1

INTRODUCTION

The latest developments in wireless communication have ushered in a new era in telecommunications to meet users' requirements for higher data rates. Applications such as the Massive Internet of Things (MIOT), enhanced cellular communications for industrial applications and cellular subscribers require high data rates in the range of gigabits per second (Gbps) [1, 2]. Fifth-generation (5G) wireless communication increases data rates by utilizing higher bandwidth than Fourth-generation (4G) communication. Furthermore, millimeter wave (mm-wave) communication offers low multi-path fading and improved spectral efficiency, as compared to the previous communication domains [3]. The 3rd Generation Partnership Project (3GPP) has already allocated several bands in the mm-wave spectrum [4]. In particular, 28 GHz bands, namely n257, n258, and n261 are designated for cellular applications. The 28 GHz band, as the pioneer 5G band, is attracting the attention of academia and industry as it is globally harmonized and reduces device manufacturing complexity. However, a higher absorption rate in this frequency band leads to higher power consumption in 5G communication systems [5]. Nevertheless, this loss can be compensated by increasing the gain level in the radiating elements of the receiver and transmitter units.

The high path loss in the mm-wave frequency regime can be addressed through the use of beam-scanning antennas. Multi-beam array antennas are able to steer the beam in spatial directions according to the given progressive phases. It is also worth mentioning that there are two different array feeding types: parallel and series. The latter is commonly used for mm-wave applications because of its simple geometry and low level of loss due to short feed line lengths [6–8]. The major disadvantage of series feeding is beam squinting, but this has been addressed in literature with various solutions such as [9–11].

Furthermore, the progressive phases can be obtained using beamforming networks (BFNs). Analog and digital BFNs are the most common types, while, hybrid and analog BFNs have been studied with an emphasis on compactness, low-loss, and cost design. These BFNs are used as an alternate to digital phase shifters to create phase differences between array antennas. Among the passive BFNs, lens-based and circuit-based BFNs have been commonly used in 5G applications such as the Rotman lens, Butler matrix (BM), Nolen matrix, and couplers [12–17]. Furthermore, microstrip and surface integrated waveguide (SIW) are among the most common hybrid and passive beamforming network topologies used in 5G applications [18–23].

BFNs are generally comprised of several digital or passive microwave circuits. Most commonly, digital BFNs employ active digital phase shifters at the input of arbitrary N×M array antennas to steer the beam in multiple directions. A sub-degree precision phase shift error can be achieved in this type of BFN. For instance, in [24], a 2-bit BiCMOS switched-bit phase-shifter, with a resolution of 45°, was presented for 5G mobile handset applications. Although this design has a phase error of less than 10°, the insertion loss (IL) was reported to be a relatively high value of 9.5 dB at 27 GHz. Similarly, in [25] a SIGe BiCMOS digitally tuned differential reflective loads phase shifter (RTPS), with an insertion loss of approximately 5 dB at 28 GHz was proposed. Even though the level of insertion loss of this model is lower than that reported in [24], the high fabrication cost and high IL value remain a concern. Consequently, it has been suggested that phased array may not be the best choice for 5G cellular communication because of their design complexity, high insertion loss, and high fabrication cost [26, 27].

In [13], a Rotman lens operating at 28 GHz was proposed resulting in an overall loss of 10.2 dB. This two-layer design generates 7 beams, with a peak gain value between 3.6 and 9.4 dBi and coverage of ±30°. This proposed design has 8 dummy ports and 7 beam ports, while the number of feed ports is reduced to 1 using a single-pole four throws (SP4T) switch. Although the design proposed in [13] (with a single-port feed network) has low complexity, it may not be suitable for 5G applications; due to the low overall gain level caused by high total losses in the system and a low beam coverage angle. To improve these limitations, a three-layer Rotman lens operating at 26 GHz and utilizing phase gradient transmission lines (PGTLs) was proposed in [12]. This design has 8 beam ports and 4 dummy ports. The 8 beams were generated with a coverage of ±56° and a reported gain value of 14 to 15.5 dBi. However, the high complexity in fabricating this design leads to a higher cost, while the higher number of ports requires a more complex feed network, prior to the BFN.

On the other hand, the 4×4 BM in [14] generates 4 beams with coverage angle

ranging from -16.2° to 12.6° and gain values in the range of 15.74 to 17.87 dBi. Even though this design improved the gain value for each beam, a fewer number of beams was generated with narrow coverage. In [15], a two-layer SIW 5×8 BM was proposed, which operates at 29 GHz with 5 beams, and $\pm 60^\circ$ beam coverage. This design provides higher beam coverage but with the drawback of a more complex and expensive method which is only generating 5 beams.

Moreover, as [28] also put forward, while the fabrication cost of SIW designs is higher, the measured gain values for SIW and microstrip technologies in the Ka-band are comparable. Even though the SIW designs have better performance and are more robust, once the dielectric loss is taken into account, they may have a higher loss than expected. Moreover, spacing between radiating elements increases in corporate topologies, which brings up the necessity of using microstrip technologies as part of the feeding network; hence, a mandatory transition from SIW to microstrip causes extra loss in the network.

Hence, in part of this thesis work [29], low-cost array antennas with corresponding BFNs were designed and implemented using microstrip technology. The proposed design operates at 28 GHz and consists of two branch-line couplers (BLCs) and one 4×4 BM as a BFN with two 2×10 and one 4×10 tapered rectangular array antennas as the radiating elements. A novel feeding technique, without the increase in the number of feeding ports, was used to produce 3 additional beams for 4×4 BM and 1 additional beam for the BLC. The special placement of the BLC and 2×10 array antenna, perpendicular to the sides of the BM, results in higher angular coverage. The final design can generate 13 beams with varying peak gain from 11.2 to 14.1 dBi and a coverage angle of $\pm 138^\circ$, while the gain value remains above 10 dBi. The proposed design was fabricated on a Rogers Corporation RO4003C with 0.203 mm thickness, $\epsilon_r = 3.55$, and $\tan\delta = 0.0027$.

Additionally, this work presents an elliptical [30] and a novel slot-loaded unit element design and corresponding array antennas operating at 28 GHz. These designs are used to improve the overall radiation bandwidth of the design and tackle the beam squinting issue in the band of interest.

The organization of this thesis is as follows; Chapter 2 will be introductory to the concept of the antenna, array antennas, and beamforming networks. Chapter 3 discuss the beamformers' topologies and design of utilized antenna arrays and explains the final system design which is used in this work, Chapter 4 presents the measurement results together with the fabrication process, and Chapter 5 will conclude the thesis.

Chapter 2

BACKGROUND

This chapter first explains an overview of the final proposed system (Section 2.1), discusses the concept of microstrip antennas (Section 2.2), array theory, and general design considerations in array antennas (Section 2.3), and continues with a summary of the beamforming networks (Section 2.4).

2.1 Final System Overview

The final system design is fabricated on 0.203 mm thick RO4003 board with dimensions of $90 \times 45 \times 11$ mm^3. This system consists of two branch line couplers (BLC) on perpendicular sides and a Butler matrix (BM) on the main side. These beamforming networks (BFN)s are connected to their corresponding Chebyshev tapered $N \times 10$ antenna arrays, N being 2 for BLCs and 4 for BM. The final system is shown in Figure 2.1. Each BLC creates 3 beams with an additional 1 extra beam as compared to the conventional BLCs, and the BM on the main side generates 7 beams with 3 additional beams as compared to conventional BM. The final system can generate 13 different beams because of the novel feeding method as shown in Figure 2.1 and has a wider beam coverage of $\pm 138^\circ$ due to the unique placement of the BLC perpendicular to the sides. The final design beams have varying peak gain from 11.2 to 14.1 dBi.

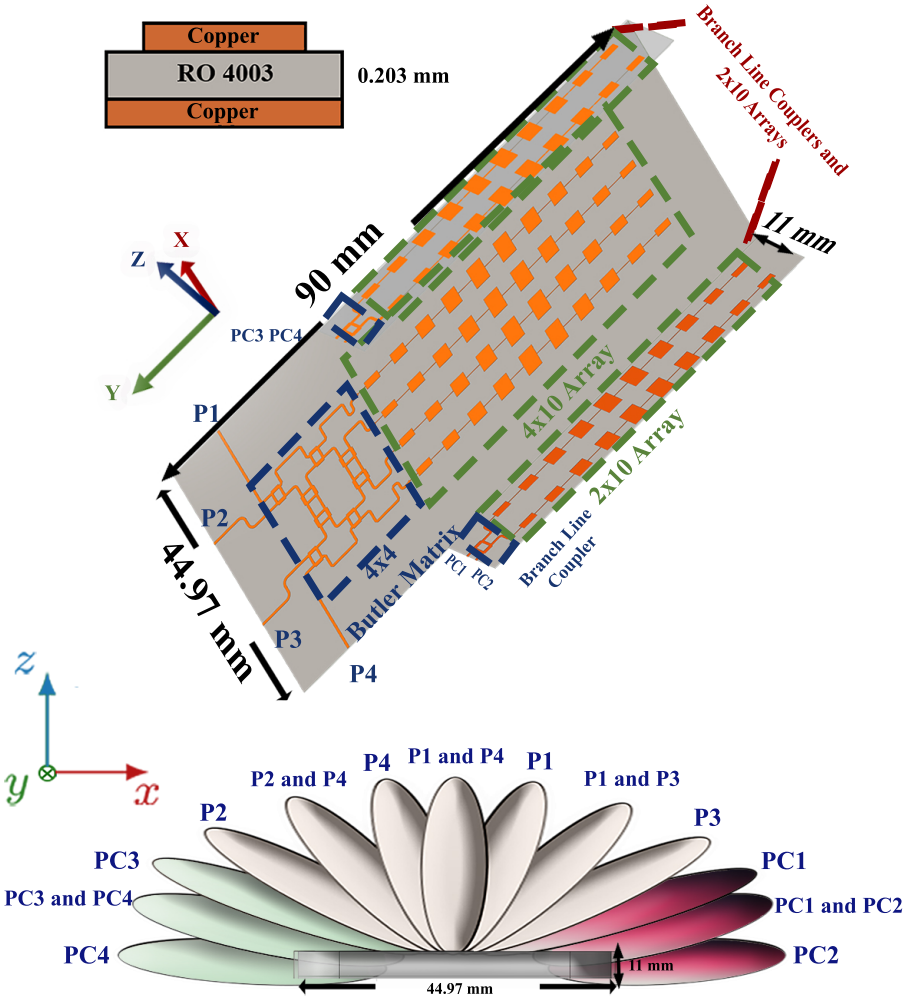

Figure 2.1 Proposed antenna system and its corresponding generated beams for two branch-line couplers with 2×10 array antennas on the edges and a Butler matrix with 4×10 array antennas on the main side.

2.2 Microstrip Antennas

Microstrip antennas consist of a thin metallic strip or patch above a ground plane and a substrate, as shown in Figure 2.2 [31]. Moreover, a rectangular patch antenna can be designed with the following parameters as shown in Figure 2.3. Once the material properties such as the dielectric constant of the substrate (ϵ_r) and the height of substrate (h) are defined; specifying the resonant frequency (f_r), W and L can be obtained from (2.1) - (2.4) [31].

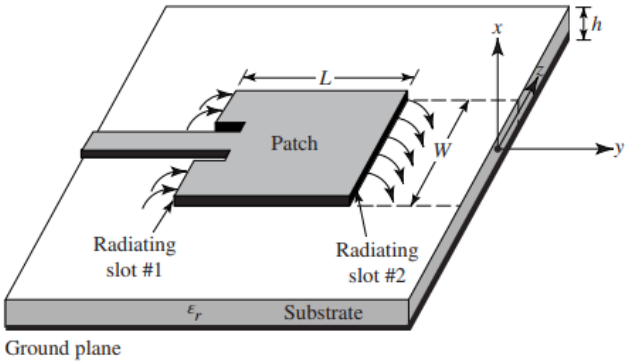

Figure 2.2 A general design of the microstrip antenna and the common definition of the design various parameters [31].

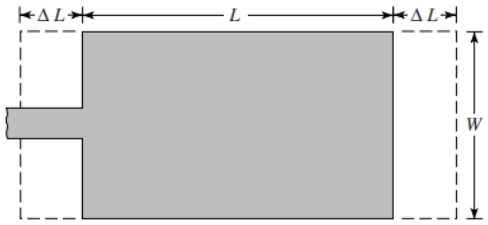

Figure 2.3 The design parameters for a microstrip rectangular patch antenna [31].

for $W/h > 1$

$$\epsilon_{reff} = \frac{\epsilon_r + 1}{2} + \frac{\epsilon_r - 1}{2}[1 + 12\frac{h}{W}]^{-1/2} \tag{2.1}$$

$$W = \frac{1}{2f_r\sqrt{\mu_0\epsilon_0}}\sqrt{\frac{2}{\epsilon_r + 1}} \tag{2.2}$$

$$\frac{\Delta L}{h} = 0.412\frac{(\epsilon_{reff} + 0.3)(\frac{W}{h} + 0.264)}{(\epsilon_{reff} - 0.258)(\frac{W}{h} + 0.8)} \tag{2.3}$$

$$L = \frac{1}{2f_r\sqrt{\epsilon_{reff}}\sqrt{\mu_0\epsilon_0}} - 2\Delta L \tag{2.4}$$

Next, impedance matching might be necessary due to the high impedance of the patch antenna ($\approx 300\ \Omega$). One of the standard matching techniques in this domain is quarter wavelength impedance matching, as shown in Figure 2.4. Furthermore, Z_c is the input impedance of the quarter wavelength transmission line, Z_l is the characteristic impedance of the line, and R_{in} is the impedance of the patch antenna as shown in Figure 2.4.

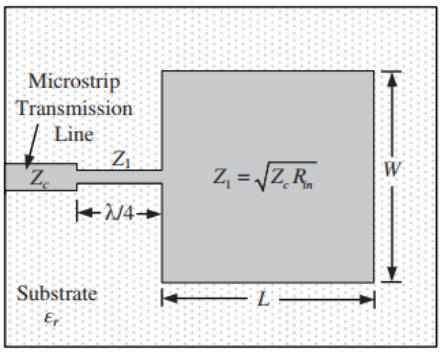

Figure 2.4 Rectangular patch antenna and corresponding quarter wavelength impedance matching [31].

The approximated normalized radiation pattern of a rectangular microstrip patch antenna can be obtained from (2.5) - (2.7) [32]. Moreover, the calculated and the simulated normalized pattern for a microstrip rectangular patch antenna ($f = 28$ GHz, $L = 3.5$ mm, $W = 2.68$ mm) is shown in Figure 2.5.

$$f(\theta,\phi) = \frac{\sin[\frac{\beta W}{2}\sin\theta\sin\phi]}{\frac{\beta W}{2}\sin\theta\sin\phi}\cos(\frac{\beta L}{2}\sin\theta\cos\phi) \tag{2.5}$$

$$E_\theta = \cos\phi f(\theta,\phi) \tag{2.6}$$

$$E_\phi = -\cos\theta\sin\phi f(\theta,\phi) \tag{2.7}$$

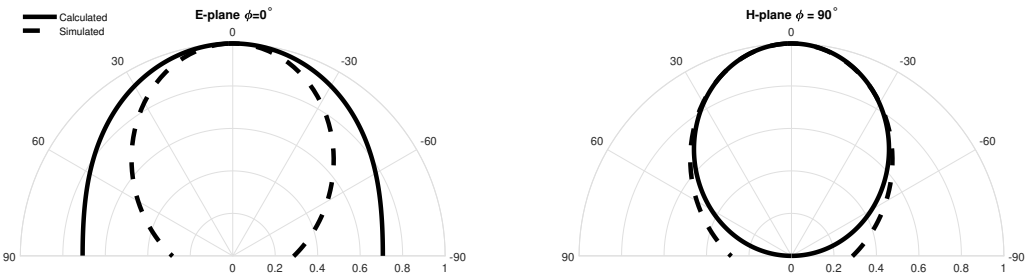

Figure 2.5 Normalized radiation pattern of a patch ($f = 28$ GHz, $L = 3.5$ mm, $W = 2.68$ mm).

2.3 Array Antennas

The array antennas have been used in various applications, as in the radar and communication systems in which highly directive characteristics are demanded [33]. Compared to the mechanically reconfigurable antennas, namely aperture antennas, electrically beam-steerable antennas have the advantage of producing various beams electrically much faster and more precisely. Array antennas generally consist of multiple identical and stationary unit elements [31, 33].

The radiation pattern of an antenna array can be defined according to its geometrical configuration, the displacement between elements, excitation, and the individual radiation pattern of their unit elements [31]. Moreover, it is possible to steer the beams in a specific direction by introducing phase variation, time delay, or even change in the amplitude in the arrays [31, 33–35]. Nevertheless, one of the common practices is to generate the beam by adjusting the phase between the adjacent array elements, as shown in Figure 2.6 [36]. These types of array antennas arise a particular category of arrays, defined as phased array antennas (PAA). It can be seen from Figure 2.6 which shows a scanned beam directed to a specific spatial direction, θ, once the phase between array elements adjusts accordingly as $\Delta\phi$. This adjustment will result in the coherent addition of elements' signals. Moreover, the progressive phase is obtained by introducing phase shifters after the power distribution network as illustrated in Figure 2.6. The phase value is $\Delta\phi = \frac{2\pi}{\lambda} d \sin\theta_0$, where d is the inter-element spacing, λ is wavelength and θ_0 is the direction of the scanned beam.

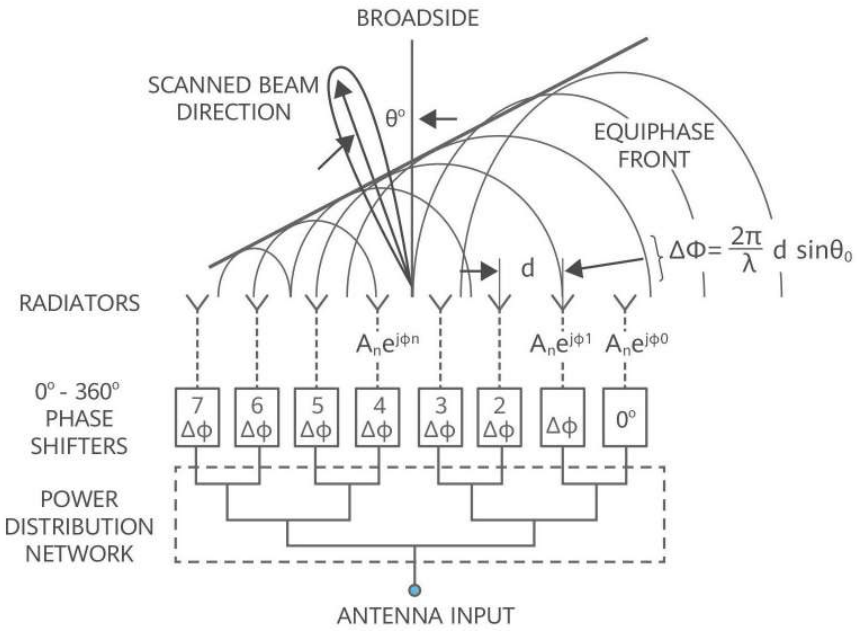

Figure 2.6 Phase difference and scanned beam direction of an array towards a radiating surface [36].

Furthermore, the phased array theory discusses the theory related to the synthesis of PAA' pattern, along with the consideration of the individual elements' amplitude, spacing, and the progressive phase [31,33–35]. Similarly, the beam scanning property of the arrays can be employed by this concept. A generalized array configuration is shown in Figure 2.7. In this configuration, the individual array placement is arbitrary. However, the orientation of each element is assumed to be the same. Each of these N elements is considered to have an identical element pattern $f(\theta, \phi)$ in the far-field, and mutual coupling between the elements is disregarded [33].

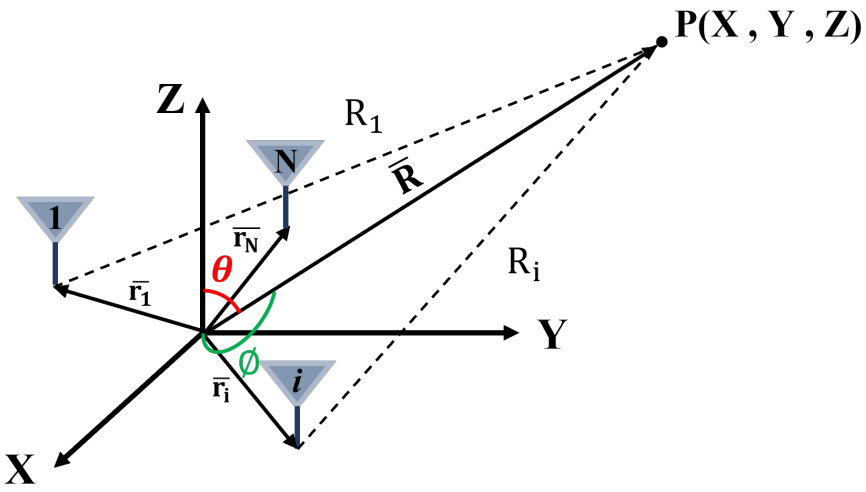

Figure 2.7 A generalized array antenna configuration and corresponding parameters in a 3-D space [33].

Obtained by the superposition principle, the (2.8) can be used to calculate the total E-field pattern of the array antenna with the identical element pattern. In this equation, the R_i terms are approximated for the magnitude as |R| and as in the (2.9) for the exponential terms.

$$E(r) = f(\theta, \phi) \frac{e^{-jk_0 R}}{4\pi R} \sum_{i=1}^{N} a_i e^{+jkr_i \cdot \hat{r}} \tag{2.8}$$

$$R_i = R - r_i \cdot \hat{r} \tag{2.9}$$

Moreover, the $k = 2\pi/\lambda$ in (2.8) is the wave constant ($\lambda = \frac{c}{f}$), and a_i is the amplitude of the corresponding element in the array. Omitting the unit element pattern (i.e., define the antenna elements as an isotropic radiator), one can define the array factor as in the (2.10).

$$AF(\theta,\phi) = \sum_{i=1}^{N} a_i e^{+jkr_i \cdot \hat{r}} \tag{2.10}$$

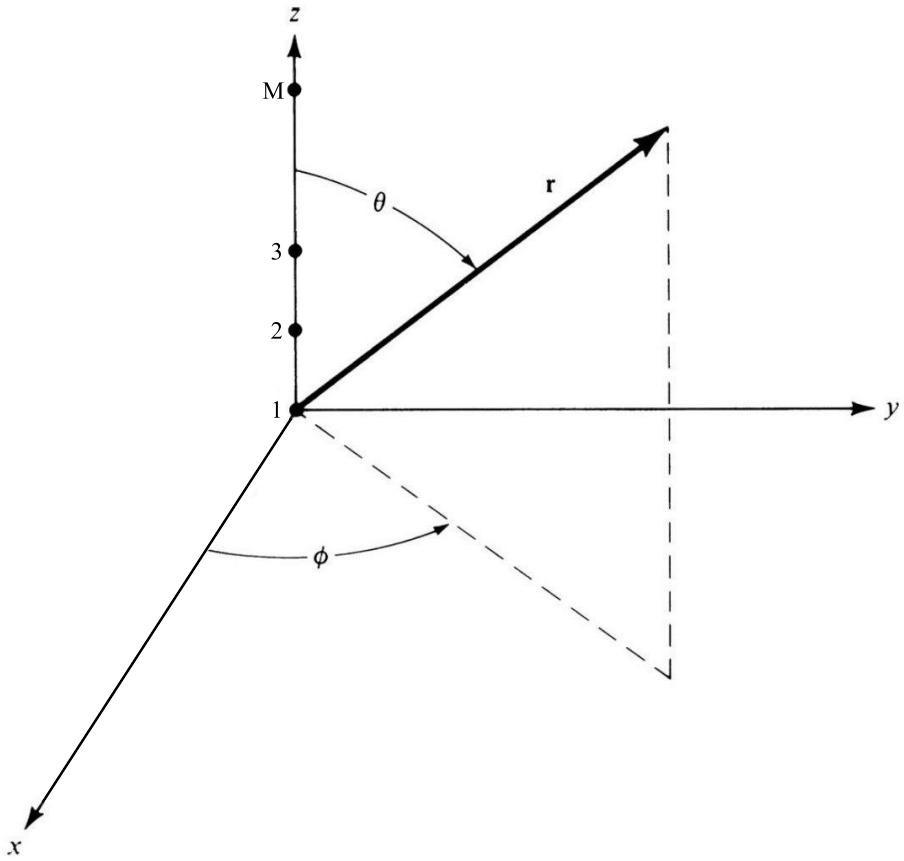

Figure 2.8 Linear array of N isotropic elements positioned along the z-axis [31].

Likewise, the linear array can be defined as a unique type of array in which elements are positioned with uniform spacing and may have a uniform or non-uniform amplitude, and an array with identical elements' amplitude and progressive phase is referred to as a uniform array [31].

$$AF(\theta,\phi) = \sum_{i=1}^{N} a_i e^{+j(i-1)\psi} \tag{2.11}$$

Following by equation (2.10) a uniform linear array place on the z-axis with different amplitude as shown in Figure 2.8 has array factor in the form of (2.11), where $\psi = kd\cos\theta + \alpha$, and α is defined as progressive phase excitation, a_i as elements amplitude and d as the inter element spacing between the array elements.

2.4 Beamforming Networks

The directive antennas' coverage area is inversely proportional to the directivity or gain of these antennas. However, a higher gain level must be provided in the 5G communication to overcome the propagation loss in these frequencies. This is illustrated in Figure 2.9 and can be verified through (2.12), where f is the frequency of the wave, r is the path length, and c is the speed of light. As a result, while wireless link sufferers from a path loss of around 82 dB at 3 GHz, this value will increase to 102 dB with the same scheme once the frequency increases to 30 GHz [37]. Moreover, atmospheric attenuation must be considered; Figure 2.10 shows the atmospheric attenuation (dB/km) at the indicated altitude hand for several exemplary weathers and air conditions.

$$pathloss = (\frac{4\pi r \times f}{c})^2 \tag{2.12}$$

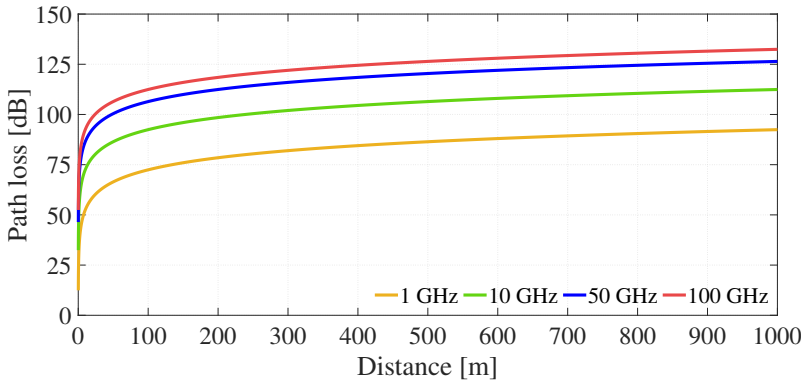

Figure 2.9 Path loss of various frequencies versus distance.

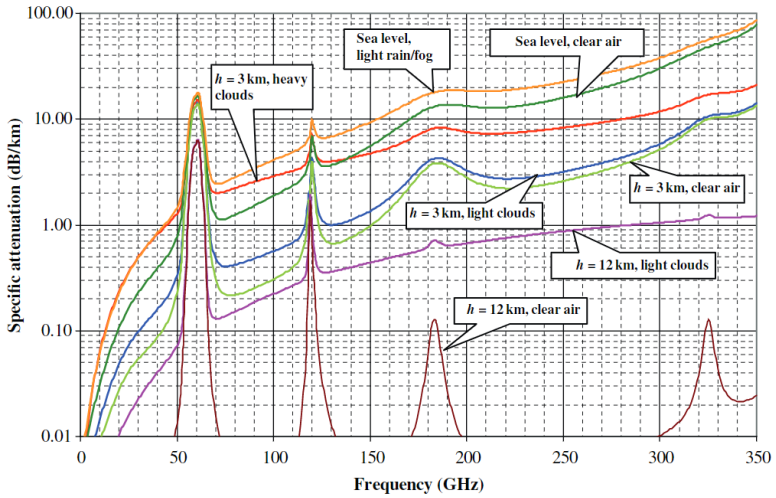

Figure 2.10 Specific atmospheric attenuation (dB/km) at the indicated altitude hand for several exemplary weather and air conditions [37].

However, a narrower beamwidth in directive antennas considers to be a disadvantage in communication applications since covering a larger area is crucial in these applications; hence to achieve a wider coverage area, it is essential to use a beamforming network (BFN). BFNs make it possible to create multiple beams, and generally integrated prior to the antenna arrays. These topologies use beam scanning capability of PAAs and, by controlling the parameters such as their progressive phase, make it possible to direct the beam to a specific spatial point [31, 33]. The beamforming architectures are available at radio frequency (RF), intermediate frequency (IF), or baseband (BB) system levels [38]. However, the focus of this thesis will be on RF beamforming, the most popular and widely employed one, which uses RF phase-shifting and PAAs to generate multiple beams.

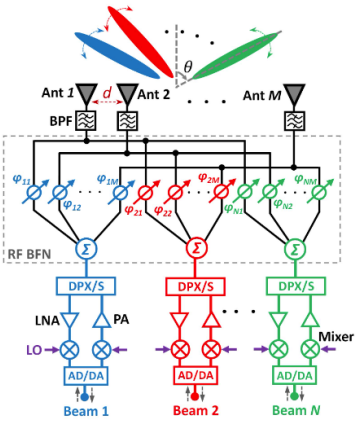

(a) Passive RF BFNs Architecture

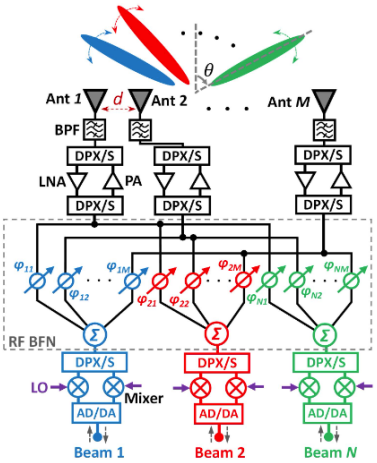

(b) Active RF BFNs Architecture

Figure 2.11 General RF BFNs system architecture [38].

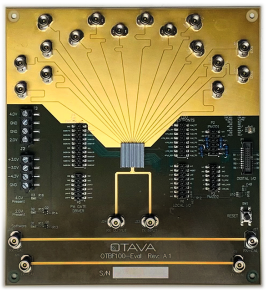

(a) Otava 5G beamformer

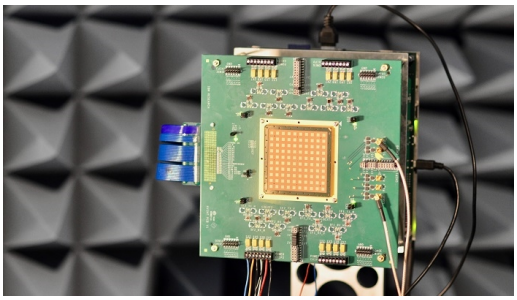

(b) IBM phased-array transceiver [39]

Figure 2.12 5G active integrated beamformers from the industry.

Two major RF beamformers categories are digital and passive, as the system architecture of them shown in Figure 2.11. Digital beamformers generally use phase shifters and active elements to direct the beam to the demanded direction (see Figure 2.11b). These beamformers achieve this by changing the progressive phase value in PAA. Hence, these beamformers have a higher precision in beam scanning angle.

However, they have the drawback of having higher insertion loss and higher cost. The higher insertion loss introduced in such a system contradicts the main objective of using the BFN in 5G communication being compensation for the higher loss in this frequency domain. Although a higher gain level might be acquired using the phased array antenna once the BFN interconnects to the array elements, the gain level will drop due to the loss introduced by the BFN [33, 40]. Moreover, several digital beamformers are already available for 5G applications, such as Otava 5G beamformer and IBM phased-array transceiver, shown in Figure 2.12.

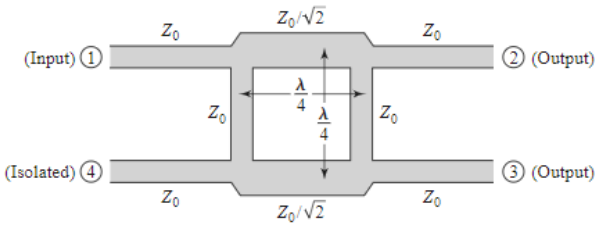

Figure 2.13 Geometry of a branch-line coupler [41].

The second type of BFNs uses passive microwave components such as power divider topologies (see Figure 2.11a). Coupler (Figure 2.13), Rotman lens (Figure 2.14a), and Butler matrix (Figure 2.14b) are some of these architectures that can be used to generate variable progressive phases for the phased array antennas. These types of beamformers generally have N input and N or more output. Once a specific input is excited, a unique progressive phase will be generated. Consequently, generating N different arbitrary beams will be possible. These beamformers attracted the community's interest as one of the possible alternatives to the digital beamformers for 5G communication because these types of BFNs are low cost and have a lower insertion loss than their digital opponents. Moreover, it is also possible to integrate these types of BFN with active elements such as active RF switches to reduce the input port number and control the beams digitally. In this manner, passive beamformers combined with active components can be considered hybrid beamforming networks.

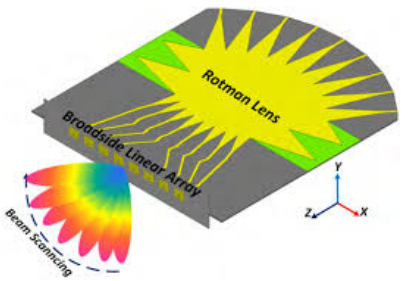

(a) A Rotman lens [42].

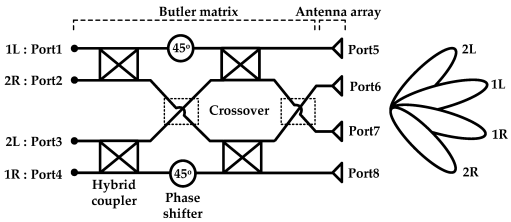

(b) A 4×4 Butler matrix [43].

Figure 2.14 Passive beamformers topologies.

Chapter 3

BEAMFORMERS AND ANTENNA DESIGN

This chapter discusses the beamformers (Section 3.1), antenna (Section 3.2) and final system design (Section 3.3).

3.1 Beamformers Design

This section's main focus is on the design of the beamformers. Section 3.1.1 explains parameters and characteristic of branch line coupler (BLC) and Section 3.1.2 present the 4×4 Butler matrix (BM)' design and evaluation of the correspondent parameters.

3.1.1 Branch Line Couplers

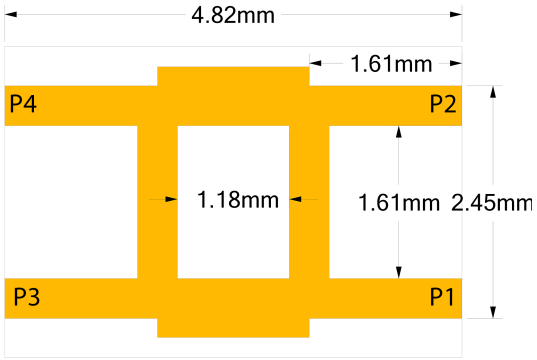

Figure 3.1 Specifications of the designed branch-line coupler.

The optimized dimensions of a single quadrature coupler, operating inside the targeted 28 GHz band, on top of the 0.203 mm thick RO4003 substrate are shown in

Figure 3.1. The simulated S-parameter values for the designed coupler are shown in Figure 3.2. Reflection coefficient and isolation levels all are below −10 dB. A near 3-dB power division was achieved, and the simulated phase differences are around 90° and deviated by a small margin of error from the theoretical phase difference values.

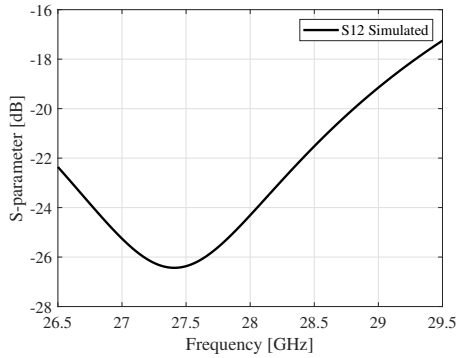

(a) Coupling

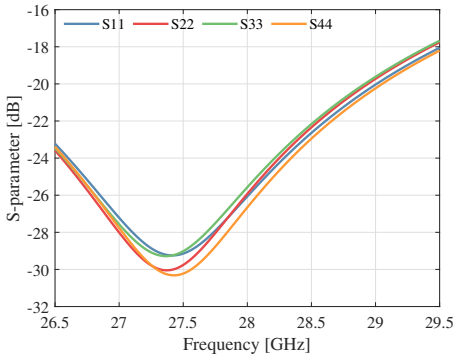

(b) Reflection Coefficients

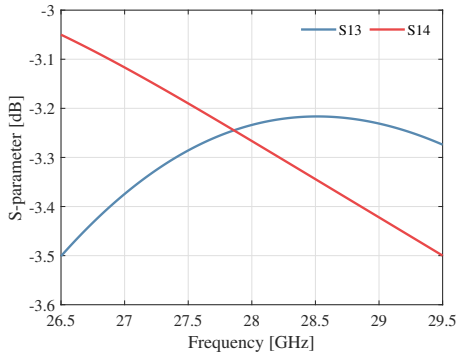

(c) Power Division

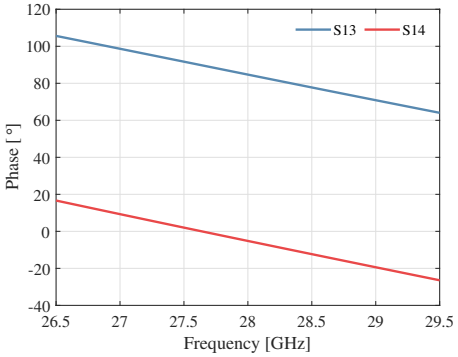

(d) Phases

Figure 3.2 Simulated S-parameter magnitude and phase values for the designed branch line coupler.

The coupler is fed from port P1, dividing the power equally between ports 3 and 4 with a −90° phase difference. This progressive phase generates a beam, designated 1L in Figure 3.3a. Similarly, the coupler is fed from port P2 dividing the power equally at the outputs but with a +90° progressive phase, and as a result, the antenna switches the beam to 1R. The last beam M as shown in Figure 3.3a, is generated by the coupler being fed from ports 1 and 2 simultaneously. The configuration of the generated beam for each of the excitation of the BLC once connected to radiators is also given in Table 3.1.

Table 3.1 Beam configuration of different excitation for the branch line coupler

State	P1 ON	P2 ON	P1 & P2 ON
Beam Direction	−18°	18°	0°

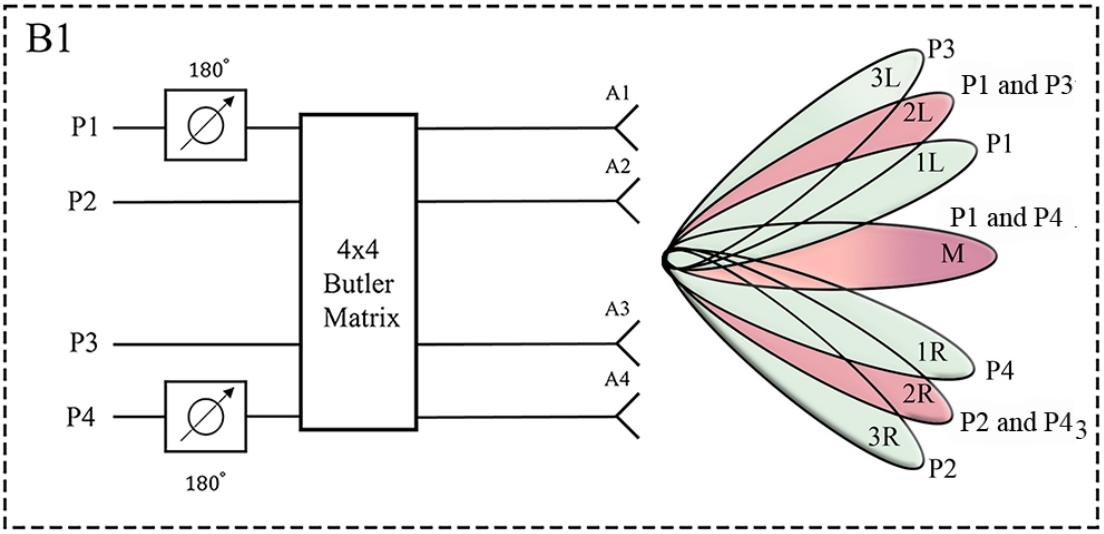

(a) 4x4 Butler matrix beamforming system

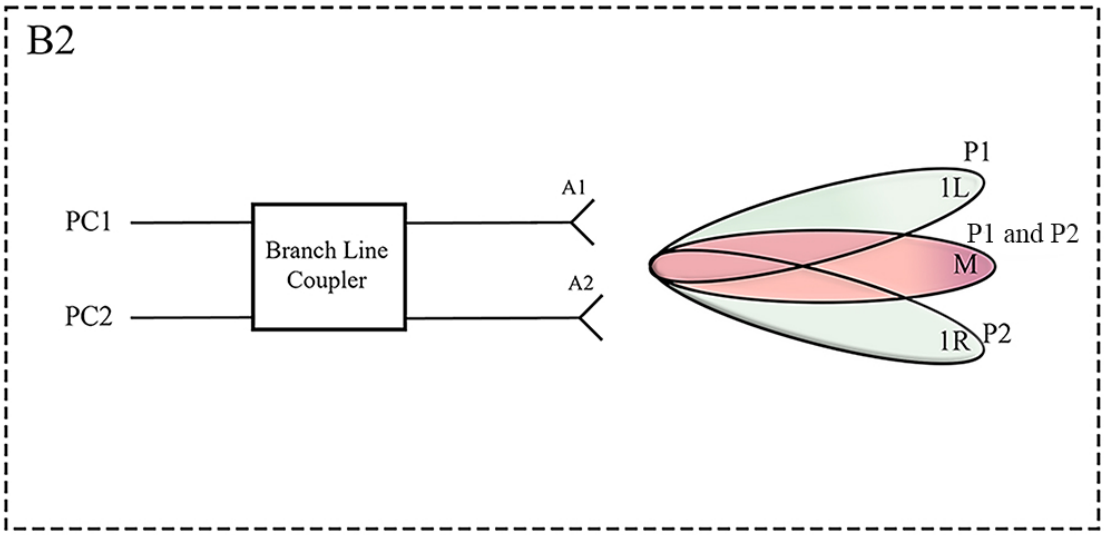

(b) Branch line coupler beamforming system

Figure 3.3 The proposed feeding method block diagram of 4×4 Butler matrix and a branch-line coupler together with corresponding array antennas.

3.1.2 4×4 Butler Matrix

The 4×4 butler matrix has four inputs (P1, P2, P3, P4) and four outputs (P5, P6, P7, P8). It is built up using four 3-dB quadrature couplers, two zero phase shifters, two cross-overs, and two transmission lines as 45° phase shifters, as shown in the Figure 3.4. The progressive phase between output ports changes depending on input port excitation, and the antenna beam is steered accordingly.

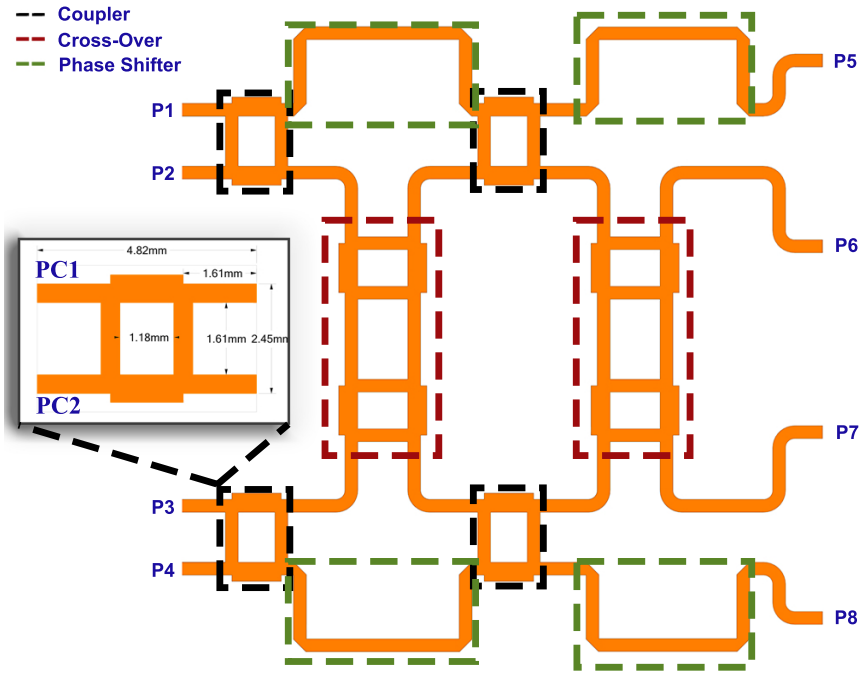

Figure 3.4 4×4 Butler matrix and branch line coupler design.

The conventional 4×4 BM can only generate 4 switched beams. However, in this work, 3 additional beams can be generated; which is achieved by adding two 180° transmission line phase shifters at the input of P1 and P4 and zero transmission line phase shifters for P2 and P3, as shown in Figure 3.3b. The phases of the output ports change for the given excitation, and it is possible to calculate the phases from the given matrix equation below. The BM output ports of these phases can be determined by the matrix and by assigning the input for the port excited as 1 for P2, P3, and as $e^{-j\pi}$ (-1) for P1 and P4 and ports that are not excited will be assigned as 0. P1 and P4 are assigned as $e^{-j\pi}$ (-1) because of the 180° phase shifter added prior to these ports. Furthermore, when individual ports P1, P2, P3, and P4 are excited 45°, 135°, −135°, −45° progressive phases are obtained. Once the additional feedings are employed, and ports are co-excited, the output phases are 0°, 90° and −90° (See Table 3.2); the output phases for these feeding configurations are as depicted in Figure 3.5.

$$\begin{bmatrix} P5 \\ P6 \\ P7 \\ P8 \end{bmatrix}^T = \begin{bmatrix} e^{-j\pi/4} & e^{-j3\pi/4} & e^{-j2\pi/4} & e^{-j4\pi/4} \\ e^{-j2\pi/4} & e^{-j0\pi/4} & e^{-j5\pi/4} & e^{-j3\pi/4} \\ e^{-j3\pi/4} & e^{-j5\pi/4} & e^{-j0\pi/4} & e^{-j2\pi/4} \\ e^{-j4\pi/4} & e^{-j2\pi/4} & e^{-j3\pi/4} & e^{-j\pi/4} \end{bmatrix} \begin{bmatrix} P1 \\ P2 \\ P3 \\ P4 \end{bmatrix}$$

Table 3.2 4×4 Butler matrix simulation progressive phase results

Feeding Port	**Simulated Progressive Phase**			**Theor. Prog. Phase**	**Average Error**
	P5-P6	**P6-P7**	**P7-P8**		
P1 (1L)	39.3°	39.3°	49.3°	45°	2.4°
P2 (3R)	-129.8°	-131.5°	-139.1°	-135°	1.5°
P3 (3L)	139.1°	131.4°	129.8°	135°	1.6°
P4 (1R)	-49.3°	-39.4°	-39.3°	-45°	2.3°
P1 and P4 (M)	-7°	0°	7°	0°	4.7°
P1 and P3 (2L)	87.4°	84.9°	90°	90°	2.6°
P2 and P4 (2R)	-90°	-84°	-87.4°	-90°	2.9°

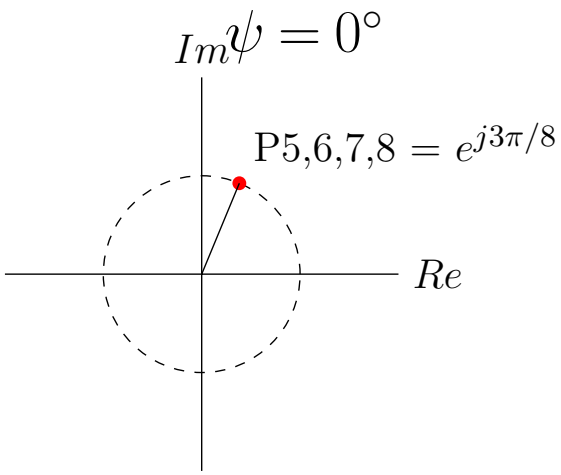

(a) P1 and P4 excited simultaneously.

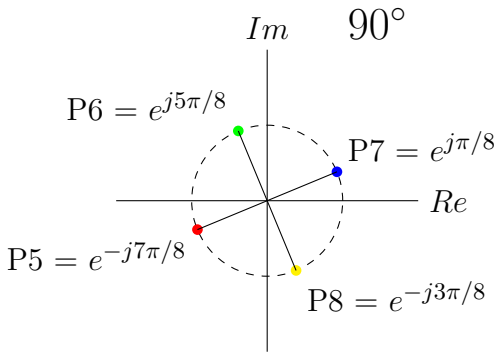

(b) P1 and P3 excited simultaneously.

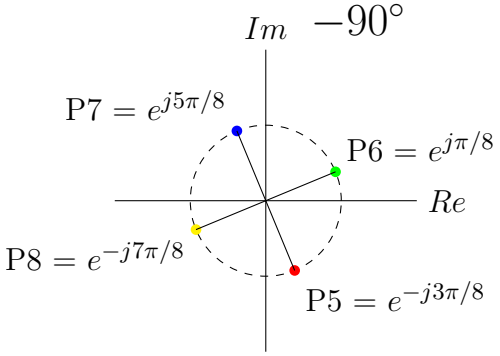

(c) P2 and P4 excited simultaneously.

Figure 3.5 4×4 Butler matrix feeding configurations for additional beams.

Table 3.2 shows the simulation results of the progressive phases generated for the 7 switched beams, together with these ideal progressive phases. For individual port excitation, when compared with the ideal progressive phase, the maximum average error was 2.4°. When ports P1, P2, P3, and P4 were excited individually, beams 1R, 3L, 3R, and 1L were generated, respectively, as shown in Figure 3.3b. In order to generate three additional beams, as shown in Figure 3.3b simultaneous two ports of the BM were excited with additional 180° phase shifters. This phase shift can be obtained by adding proper transmission lines prior to the BM. When P1 and P4 are excited simultaneously, beam M is generated with a 4.7° average error. The last two beams can be generated by exciting (P1 and P3) and (P2 and P4) in the same manner, respectively. Moreover, the ideal insertion loss of a 4×4 BM is around 6 dB which comes from two consecutive 3-dB couplers, but since cross-over couplers and extended transmission lines are added, losses of the BM increase in some of the cases as shown in Figure 3.6. In the simulation, the loss ($\sum_{j=5}^{8} |Sij|^2$, where i=1, 2, 3, 4) varied from 4.4 dB to 6.6 dB . The simulated reflection coefficient values for the 4×4 are also shown in Figure 3.7.

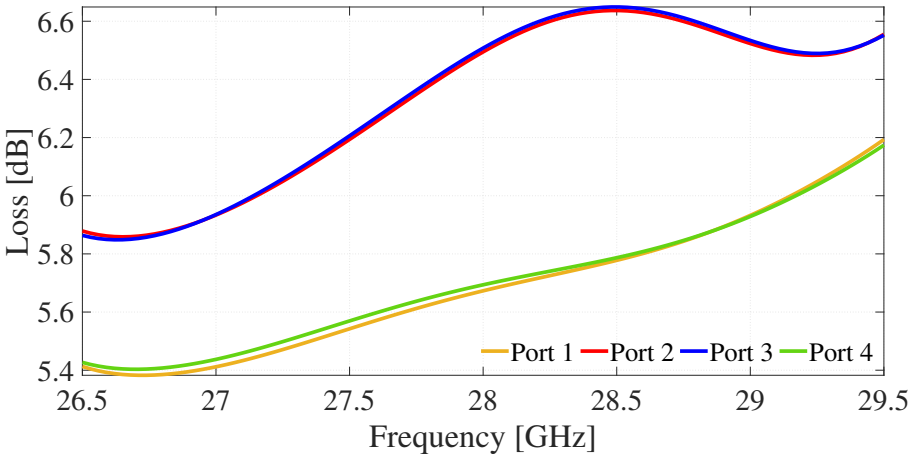

Figure 3.6 Simulated loss values for the designed 4×4 Butler matrix.

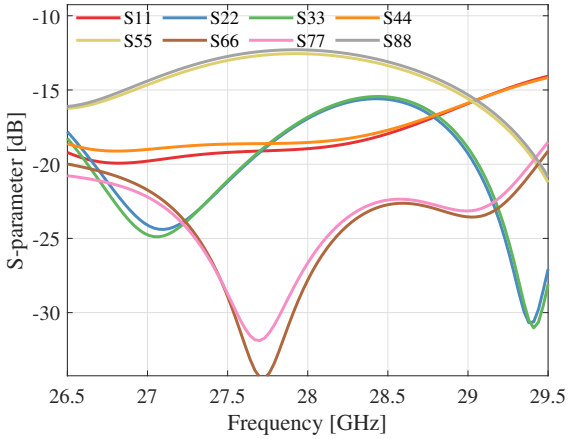

Figure 3.7 Simulated reflection coefficient values for the designed 4×4 Butler matrix.

3.2 Antenna Design

This section explains the detailed design procedure and simulation results for rectangular array antenna (Section 3.2.1), elliptical array antenna (Section 3.2.2), and slot loaded elliptical array antenna (Section 3.2.3).

3.2.1 Rectangular Antenna Array

First a unit rectangular patch element designed an optimized to operating at 28 GHz in HFSS 2021R2 as shown in the Figure 3.8.

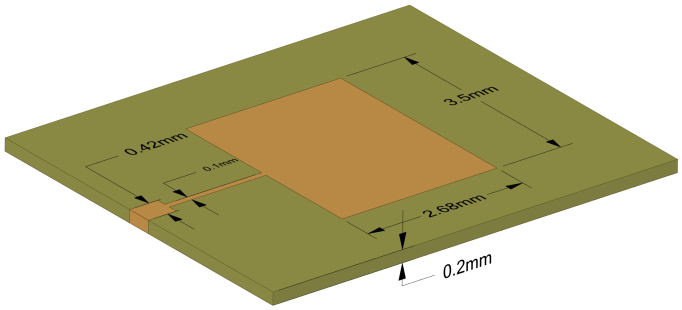

Figure 3.8 Rectangular patch antenna design.

The procedure explained in Section 2.2 is used as the initial point, and the next design is optimized. The designed unit element simulated reflection coefficient is shown in Figure 3.9, as the rectangular patch are generally narrow band it is hard to achieve a -10 dB reflection for the whole band of the interest.

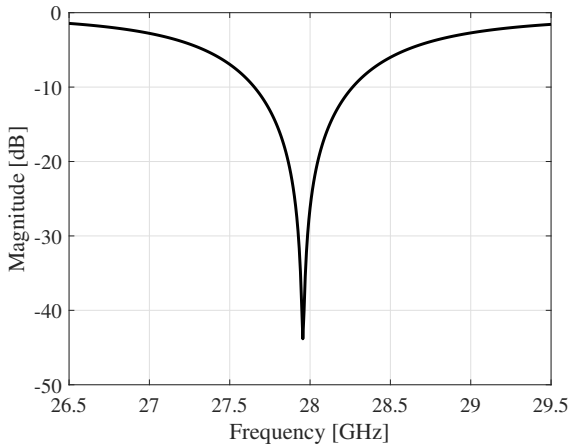

Figure 3.9 Rectangular patch simulated reflection coefficient.

The realized gain versus frequency for this antenna is also shown in Figure 3.10. After finalizing the unit element, a series fed 1×10 array was designed using this element. The designed unit element simulated reflection coefficient is shown in Figure 3.9. The realized gain versus frequency for this antenna is also shown in Figure 3.10. After finalizing the unit element, a series fed 1×10 array was designed using this element.

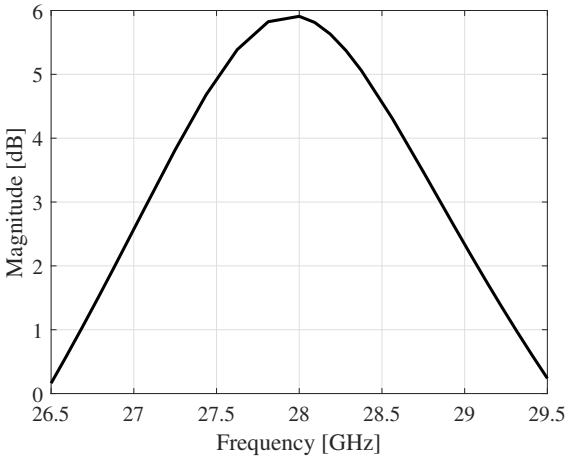

Figure 3.10 Rectangular patch simulated realized gain versus frequency.

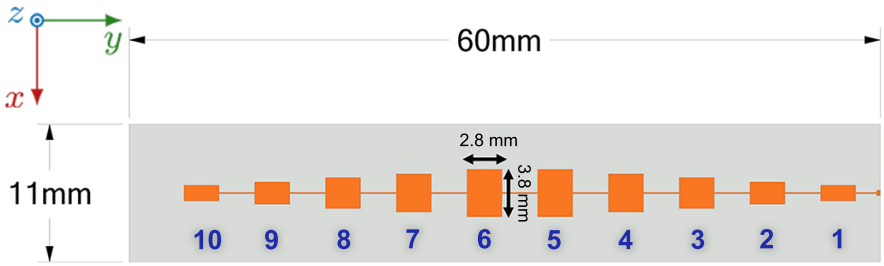

Figure 3.11 1×10 Series-Fed Chebyshev tapered rectangular array antenna design and corresponding element numbers.

Table 3.3 Tapering coefficients for elements of 1×10 array antenna

Element	1 and 10	2 and 9	3 and 8	4 and 7	5 and 6
Tapering Coeff.	0.33	0.47	0.65	0.8	1

A microstrip series fed array with 10 rectangular elements was designed and optimized to operate at 28 GHz. The final dimensions of the 1×10 array are $60 \times 11 \times 0.203$ mm^3, while the primary patch dimensions are 2.8×3.8 mm^2, as given in Figure 3.11. A tapering technique was used to reduce the sidelobe level (SLL) and related elements were tapered using the Chebyshev coefficient as shown in Table 3.3. The first five elements of the 1×10 array were chosen to be equal to the last five elements of the array, in a symmetrical fashion. The inter-element spacing of the proposed antenna was chosen as $\lambda_g/2$, a guided wavelength, which has a value of 2.85 mm after optimization.

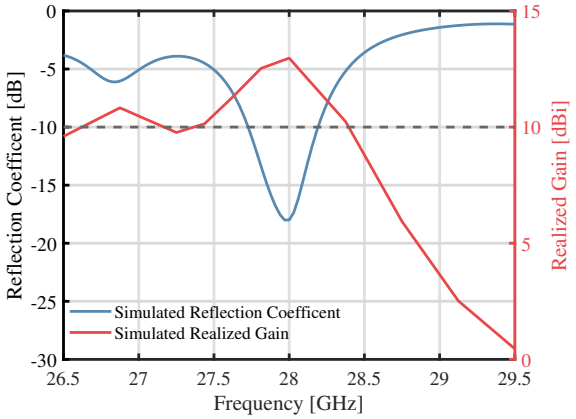

Figure 3.12 1×10 rectangular array antenna simulated reflection coefficient and realized gain versus frequency at $\phi = 0°$-plane.

The simulated reflection coefficient and realized gain at azimuth angle ($\phi = 0°$) values for the 26.5 to 29.5 GHz frequency band are shown in Figure 3.12. A minimum reflection coefficient of -18 dB occurred at 28 GHz. Meanwhile, the designed

antenna has a reflection coefficient of less than −10 dB, between 27.73 and 28.18 GHz, and a gain value of more than 10 dBi between 26.62 and 28.27 GHz. A peak gain value of 13 dBi was observed at 28 GHz. The simulated normalized E and H plane is shown in Figure 3.13 at 28 GHz. The main lobe occurs at the 4° boresight angle with a better than −10 dB SLL while this value is around −6 dB without tapering technique as compared in Figure 3.14.

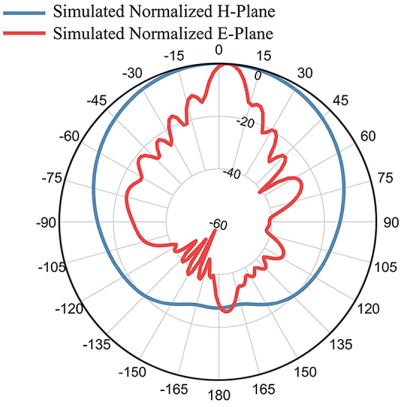

Figure 3.13 1×10 rectangular array antenna simulated normalized E and H fields at 28 GHz and $\phi = 0°$-plane.

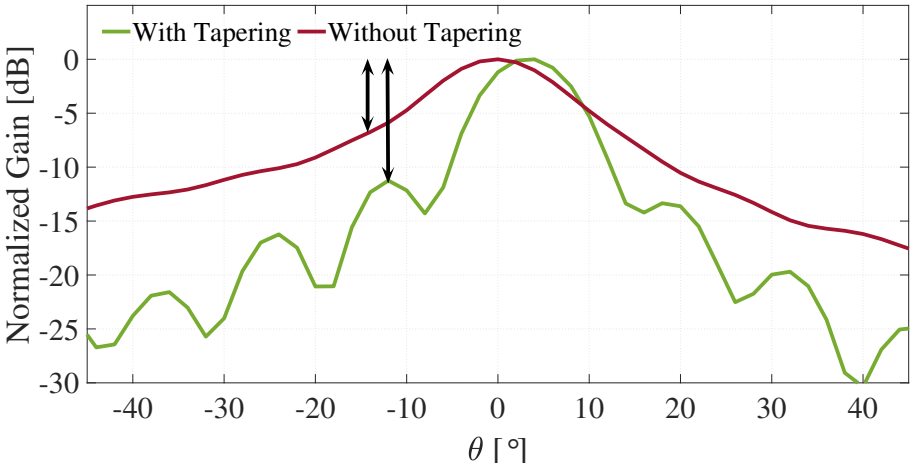

Figure 3.14 Simulated normalized gain at 28 GHz and $\phi = 90°$-plane for 1×10 rectangular array antenna with and without tapering.

3.2.2 Elliptical Antenna Array

The elliptical unit element was investigated to improve the radiation bandwidth of the unit elements in the array. For this purpose, elliptical design is optimized to operate at 28 GHz, as shown in Figure 3.15.

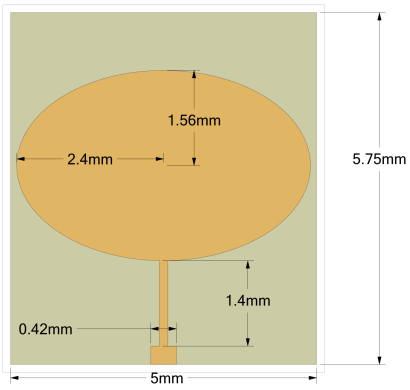

Figure 3.15 Elliptical patch antenna design.

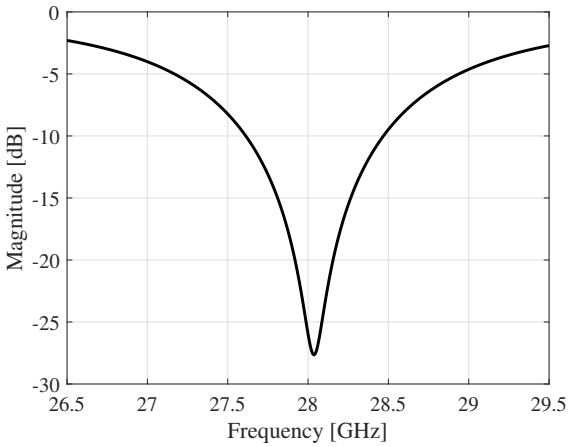

Figure 3.16 Elliptical patch simulated reflection coefficient.

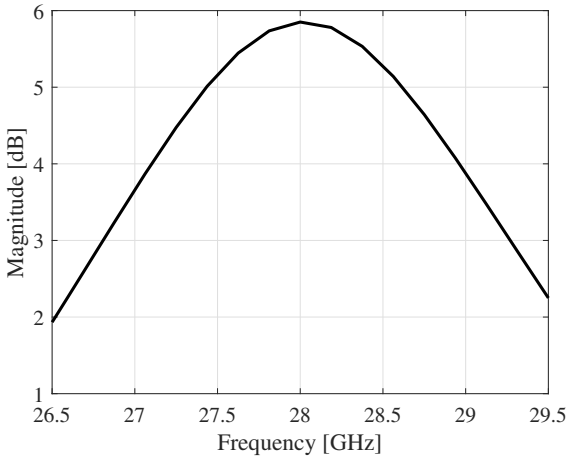

Figure 3.17 Elliptical patch simulated realized gain versus frequency.

The designed unit element simulated reflection coefficient of designed unit element is shown in Figure 3.16, the reflection coefficient value got slightly better. The realized gain versus frequency for this antenna is also shown in Figure 3.17 and it can be confirmed that these values get improved in this band.

A 1×10 series fed PAA was designed and optimized to operate at 28 GHz. As a dielectric, Rogers Corporation RO4003C with 0.203 mm thickness, $\epsilon_r = 3.55$, and $\tan\delta = 0.0027$ was used. The r1 and r2 values were assigned as 1.62 mm and 2.52 mm, respectively as shown in Figure 3.18. A symmetric design shown in Figure 3.18 was preferred to overcome beam squinting, as suggested in [9]. Next, a tapering technique was used to reduce the side-lobe level (SLL). The design was Chebyshev tapered with the individual Chebyshev binomial element coefficients [0.47,0.58,0.79,0.91,1] by adjusting the r2 dimension for each element, as illustrated in Figure 3.18.

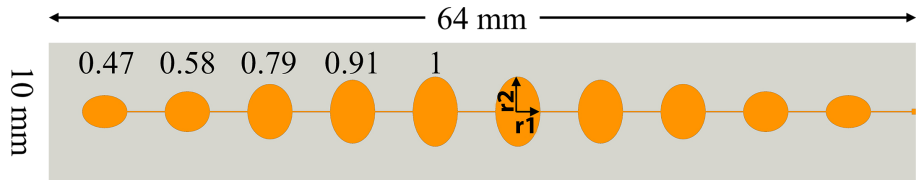

Figure 3.18 1×10 Chebyshev tapered series fed elliptic PAA design

The design is symmetrical, and the other five elements of 1×10 PAA have the same coefficients as those shown in Figure 3.18. The widths of 50 Ω and 94 Ω lines were calculated as 0.42 mm and 0.1 mm, respectively. The elliptical structure and Chebyshev tapering provide a relatively higher bandwidth since section-wise this structure can be treated as multiple sections of different dimensions as opposed to the rectangular patch in which each section has the same electrical dimensions.

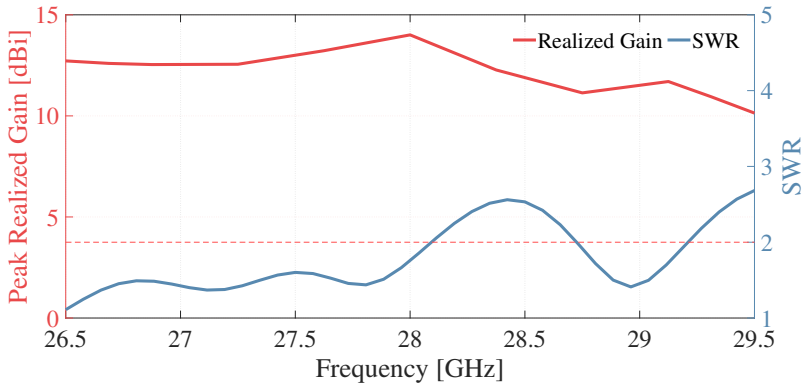

Figure 3.19 1×10 PAA design simulated SWR and peak realized gain versus frequency at $\phi = 0$

Lines with characteristic impedances of 50 Ω and 94 Ω were used to excite the design, and connect 10 elliptic elements, respectively, thus feeding them in series.

The center to center element spacing equals $\lambda_g/2$, λ_g being the guided wavelength. Further, to improve the 50 Ω matching, a line of 2.95 mm, approximately $\lambda_0/4$, was used to feed the first element, where λ_0 is the wavelength in the free space. The simulated gain of the 1×10 PAA yielded a main lobe level of 14 dBi at 28 GHz and $\phi = 0$. The simulated standing wave ratio (SWR) and a realized gain value of the design for the frequencies within the band are shown in Figure 3.19. Peak realized gain value was above 10 dBi for the band, and the maximum gain value occurred at $\phi = 0$ for 28 GHz. The SWR value was below 2 for 63 percent of the band, while it was below 2.7 for the entire band. Beam shift in ϕ direction was observed for 1×10 PAA. Consequently, the peak realized gain values were higher than those of the realized gain for $\phi = 0$ in the band. Moreover, the main lobe occurs at the 0° boresight angle with a better than −11 dB SLL while this value is around −10 dB without tapering technique as compared in Figure 3.20.

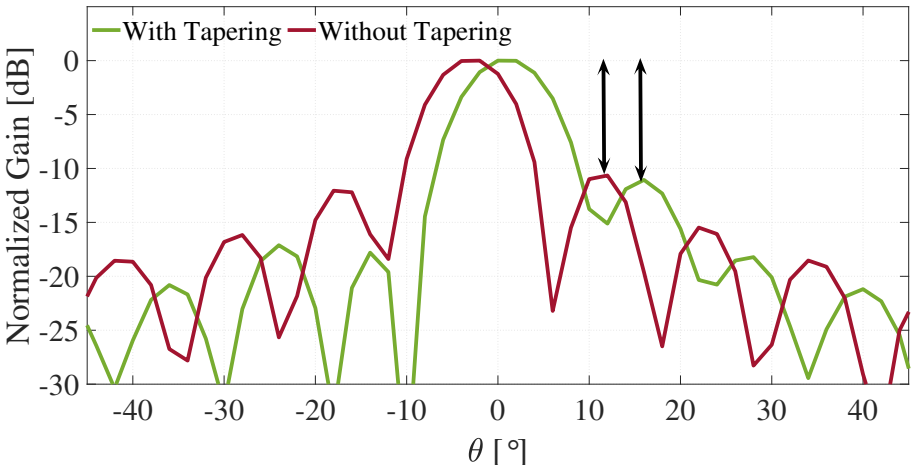

Figure 3.20 Simulated normalized gain at 28 GHz and $\phi = 90°$-plane for 1×10 elliptical array antenna with and without tapering.

3.2.3 Slot Loaded Elliptical Antenna

The improved radiation performance of the antenna array with elliptical elements was investigated more. A novel slot-loaded elliptical microstrip antenna unit element (see Figure 3.21) and the corresponding 1×5 array (see Figure 3.23) were proposed to achieve flat gain for the band of interest and overcome the beam squint issue. Moreover, for ease in comparison, in this section, the slot-loaded antenna performance parameters are illustrated together with the one for the rectangular and elliptical antenna. The designed unit element simulated reflection coefficients for the antennas are shown in Figure 3.22a. The realized gain versus frequency for this antenna is also shown in Figure 3.22b

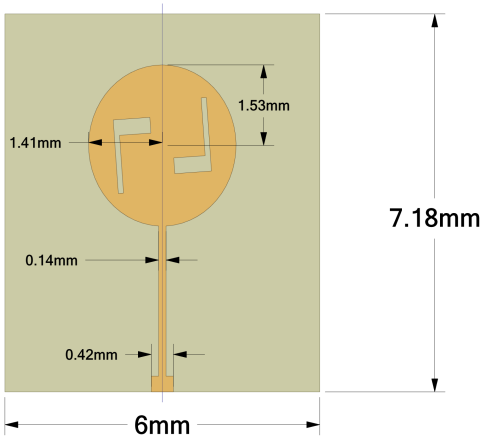

Figure 3.21 Slot loaded elliptical patch antenna design.

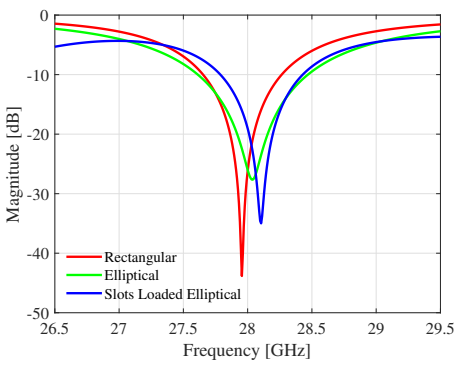

(a) Simulated reflection coefficient.

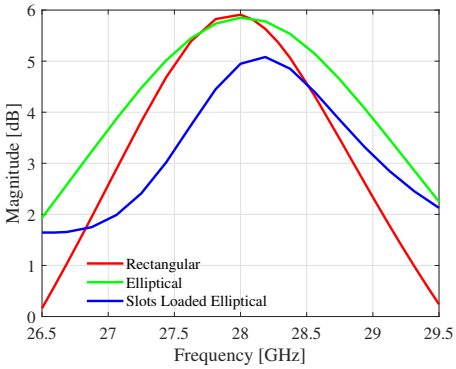

(b) Simulated realized gain.

Figure 3.22 Slot loaded elliptical patch antenna design simulated gain and reflection coefficient.

The designed unit element simulated reflection coefficients for the antenna arrays are shown in Figure 3.24a. The realized gain versus frequency for this antenna is also shown in Figure 3.24b

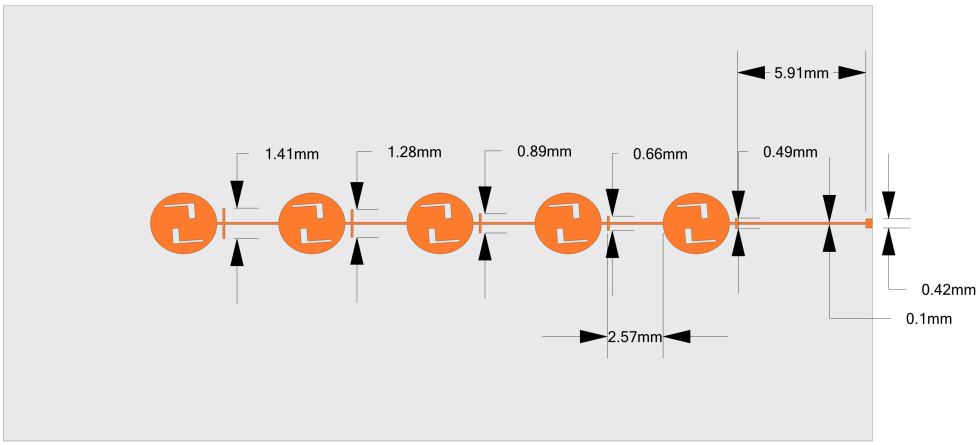

Figure 3.23 Slot loaded elliptical patch antenna design.

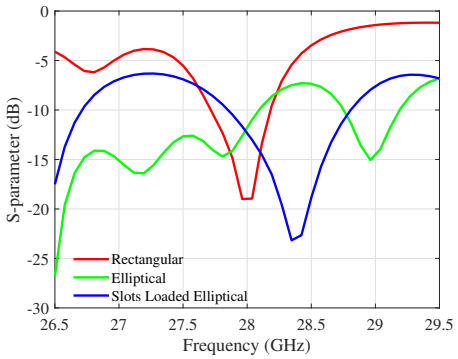

(a) Simulated reflection coefficient.

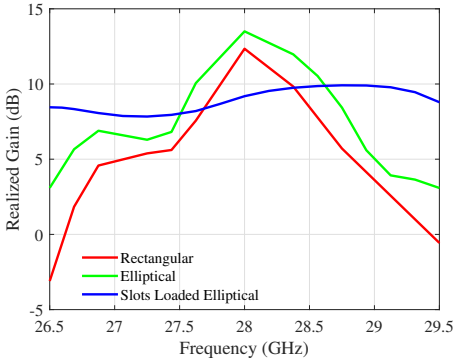

(b) Simulated realized gain.

Figure 3.24 Slot loaded elliptical array antenna design simulated gain and reflection coefficient.

3.3 Final Designs

This section discuss the interconnection of the array antennas and beamforming networks (Section 3.3.1, 3.3.2, 3.3.3). The final system design presented at Section 3.3.4

3.3.1 Butler Matrix and 4×10 Rectangular Array

The BM is connected to 4×10 array antennas as shown in Figure 3.25a by placing the 1×10 array antennas adjacent to each other with a distance of $\lambda_0/2$ between them, where λ_0 is the wavelength in free space. The optimized value of the spacing between the adjacent 1×10 array antennas is 6 mm.

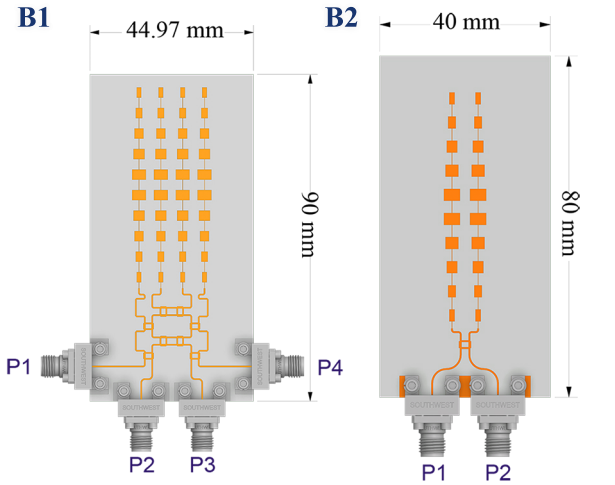

(a) Designed 2x10 PAA with BLC and port definition

(b) Designed 4x10 PAA with BM and port definition

Figure 3.25 Designed 2×10 and 4×10 array antennas with BLC and BM as BFNs and corresponding port definitions.

As mentioned earlier, the antenna system shown in Figure 3.25a can generate 7 different beam which are shown in Figure 3.26

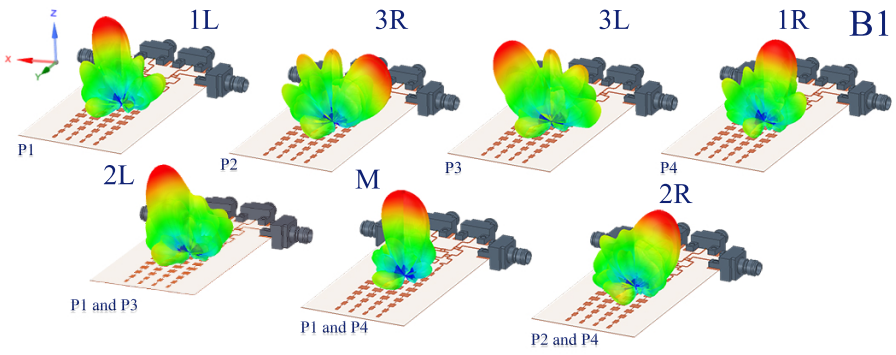

Figure 3.26 Simulated 7 beam pattern of the 4×10 array antennas and BM with 7 different excitation configuration.

3.3.2 Branch Line Coupler and 2×10 Rectangular Array

The BLC is connected to 2×10 array antennas as shown in Figure 3.25b by placing the 1×10 array antennas adjacent to each other with a distance of $\lambda_0/2$ between them, where λ_0 is the wavelength in free space. The optimized value of the spacing between the adjacent 1×10 array antennas is 6 mm in this configuration as well. Moreover, the antenna system shown in Figure 3.25b can generate 3 different beam which are shown in Figure 3.27

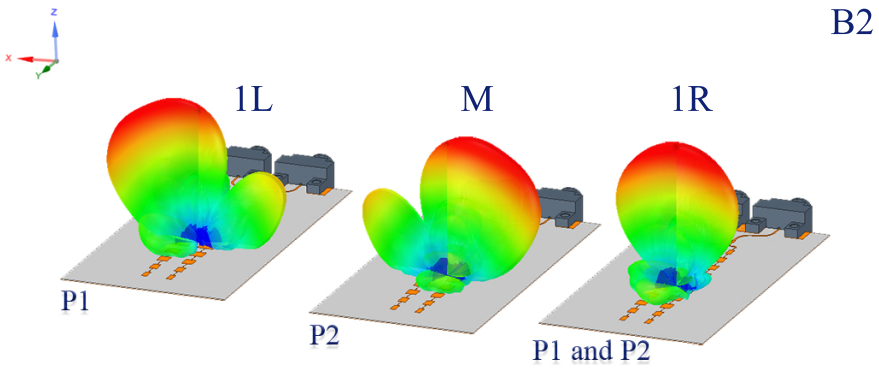

Figure 3.27 Simulated 3 beam pattern of the 2×10 array antennas and BLC with 3 different excitation configuration.

3.3.3 Branch Line Coupler and 2×10 Elliptical Array

A 2×10 PAA was created by placing two of the 1×10 arrays as shown in Figure 3.28, with around $\lambda_0/2$ inter element spacing. After optimizing the distance between the two 1×10 elements,this value was set to 6 mm. Next, a BLC was connected to the designed 2×10 PAA. This BLC generates the needed phase and amplitude excitation to produce three switched beams. The coupler was optimized to operate within the targeted 5G band; all physical parameters of the coupler are shown in Figure 3.28.

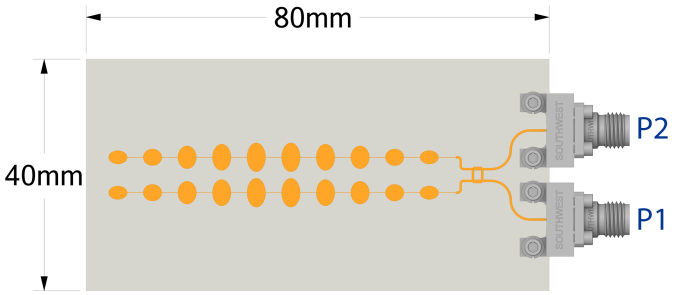

Figure 3.28 A 2×10 elliptical antenna array with BLC.

The radiation pattern of the three generated beams of the final design illustrated in Figure 3.29. 1R, M, 1L are the formed beams at $-18°$, $0°$ and $18°$ respectively.

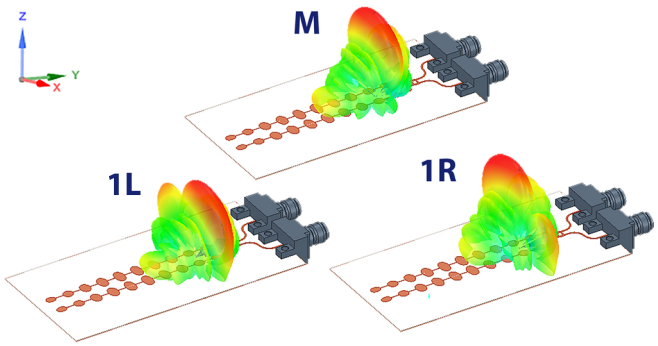

Figure 3.29 Simulated beam pattern of 2×10 PAA with BLC

The simulated peak realized gain of the 2×10 PAA and BLC for each of the excitations is shown in Figure 3.30. The realized gain value was higher than 10 dBi over the band and higher than 12 dBi from 26.5 GHz to 28 GHz. The maximum gain level occurs at frequencies around 28 GHz for all of the generated beams. Moreover, each beam had a 3-dB beamwidth of around 43°.

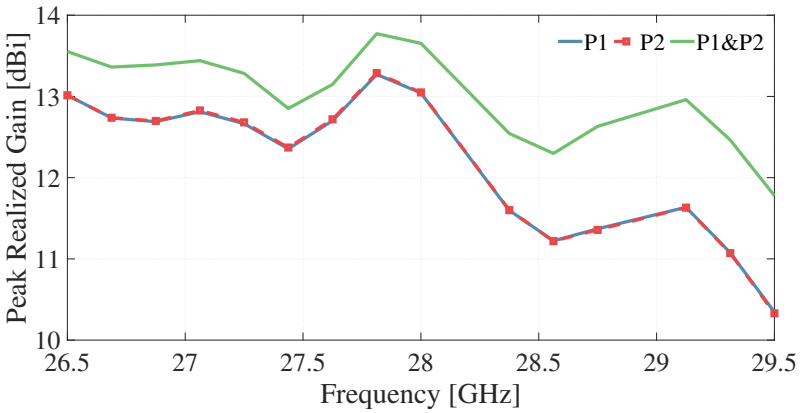

Figure 3.30 Simulated peak realized gain versus frequency of 2×10 PAA with BLC

3.3.4 Final System

The proposed design and generated beams are illustrated in Figure 3.31. This design operates at 28 GHz and consists of two branch-line couplers and one 4×4 BM as a BFN. The design consists of two 2×10 and one 4×10 tapered rectangular array antennas as the radiating elements. A novel feeding technique, without increasing the number of feeding ports, was used to produce 3 additional beams for 4×4 BM and 1 additional beam for the branch line coupler (BLC). The special placement of the BLC and 2×10 array antenna, perpendicular to the sides of the BM, results in higher angular coverage as shown in Figure 3.31. The final design can generate 13 beams with varying peak gain from 11.2 to 14.1 dBi and a coverage angle of $\pm 138°$, while the gain value remains above 10 dBi. The simulated, normalized gain pattern of the proposed antenna system at 28 GHz is given in Figure 3.32. Finally, the performance of the design evaluated comparing with the state of art designs provided in Table 3.4

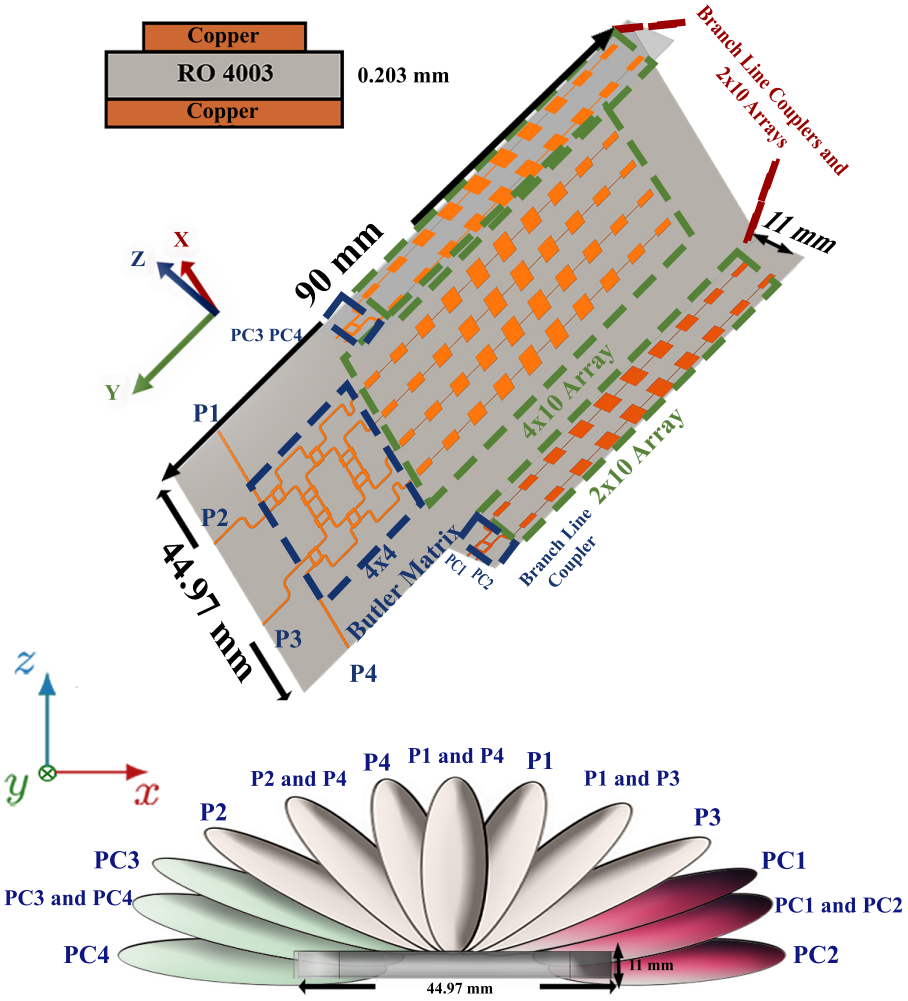

Figure 3.31 Proposed antenna system and its corresponding generated beams for two branch-line couplers with 2×10 array antennas on the edges and a Butler matrix with 4×10 array antennas on the main side.

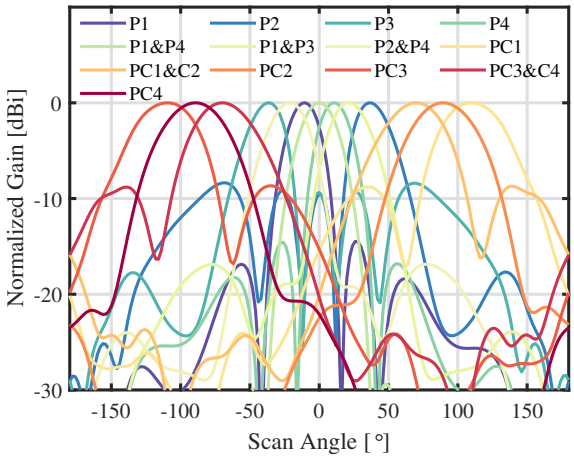

Figure 3.32 Simulated, normalized gain results of the final system versus scan angle at 28 GHz and $\phi = 0°$-plane.

Table 3.4 Comparison with previously proposed multi beam designs for 5G mm-wave applications

Ref.	Freq (GHz)	Type of System	Technology	Num. of Ports/ Beams	Beam Coverage
[14]	27.925	Single Layer 4×4 BM	Microstrip	4/4	$-16.2°$ to $12.6°$
[15]	29	Dual Layer 5×8 BM	SIW	5/5	$\pm 60°$
[44]	30	Dual Layer 4×16 BM	SIW	4/4	$\pm 30°$
[45]	38	Three Layer 4×8 BM	SIW	4/4	$\pm 36°$
[46]	60	Single Layer 4×4 BM	Microstrip	4/4	$\pm 60°$
[47]	28	Dual Layer 4×6 BM	Microstrip	4/4	$\pm 45°$
This work	**28**	**Single Layer 4×4 BM+ BLC**	**Microstrip**	**8/13**	$\pm$**138°**

Chapter 4

FABRICATION AND MEASUREMENT

This chapter discusses to the measurements results and presents the loss calculation (Section 4.1), measured scattering matrix and radiation pattern of BM and 4×10 rectangular array (Section 4.2), BLC and 2×10 rectangular array (Section 4.3) and BLC and 2×10 elliptical array (Section 4.4).

4.1 Loss Calculation

In order to have better confirmation between measurement and simulated results, individual insertion loss of the components used in the measurement are measured and taken into consideration accordingly. The results of this measurement is provided in the following manner, power divider loss (Section 4.1.1),cable loss (Section 4.1.2), and connector loss (Section 4.1.3).

4.1.1 Power Divider

SigaTek SP70203 was used as a power divider, and this component scattering matrix was measured with an Agilent PNA 5245A vector network analyzer (VNA) as shown in Figure 4.1.

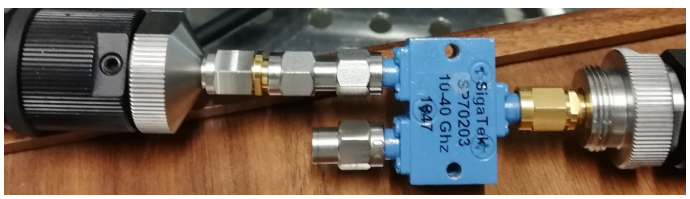

Figure 4.1 IL measurement setup of SigaTek SP70203.

Furthermore, the results of this measurement are illustrated in Figure 4.2, reflection coefficients of all of the ports have values better than −10 dB for the entire band. Moreover, the S12 and S13 values at 28 GHz are −3.44 dB and −3.39 dB, respectively.

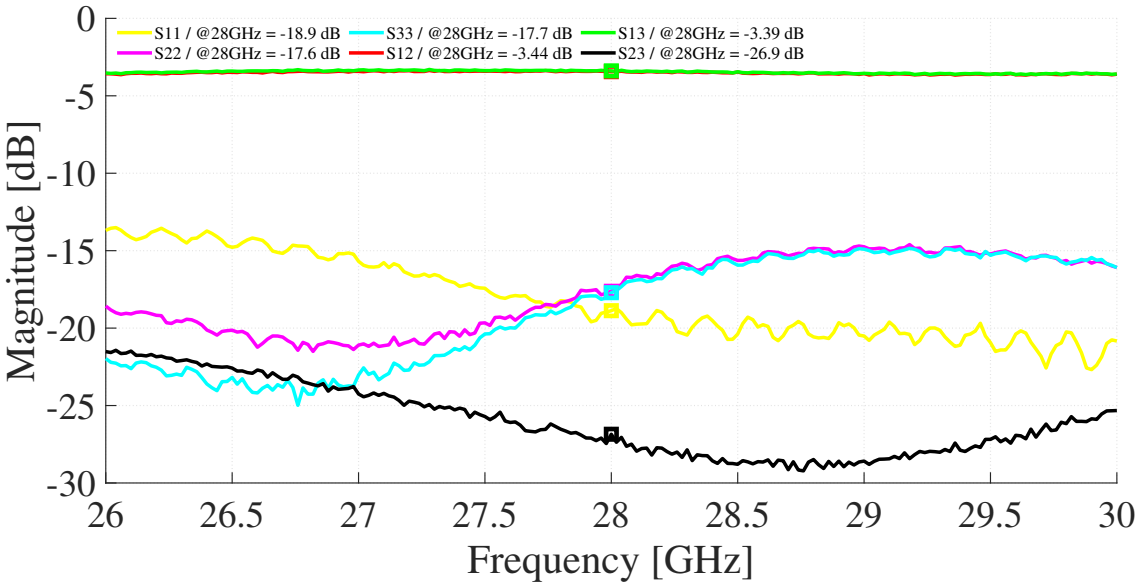

Figure 4.2 Measured scattering matrix of SigaTek SP70203.

4.1.2 Cable

Power divider connected to the designs using cables, these cables creates an extra loss in the system, for this reason, the loss of the cables used measured as well as shown in Figure 4.3 and the results of this measurement is shown in Figure 4.4 and Figure 4.5. The reflection coefficients of all of the ports have values better than −10 dB for the entire band. Moreover, the measured IL value at 28 GHz is 0.68 dB.

Figure 4.3 IL measurement setup of cables.

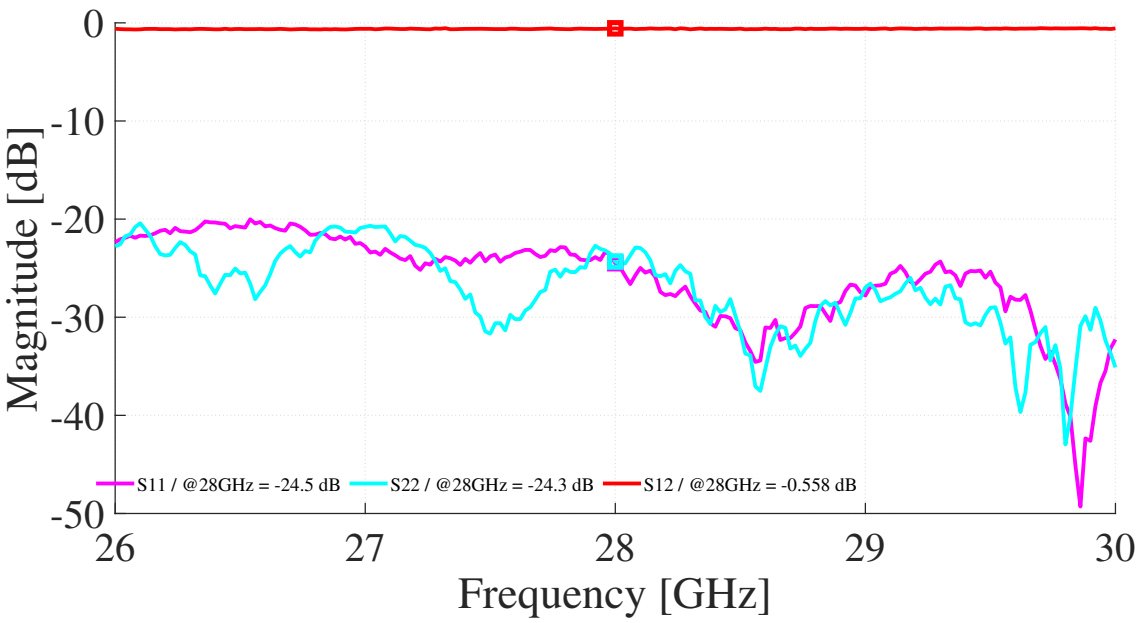

Figure 4.4 Measured scattering matrix of cables.

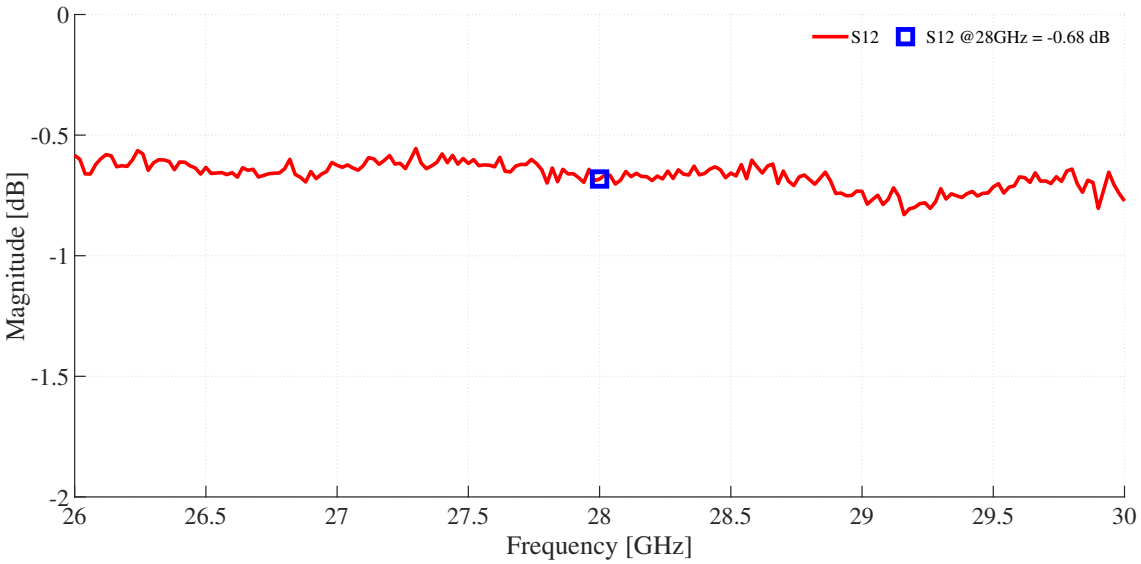

Figure 4.5 Measured IL of cables.

4.1.3 Connectors

The Southwest end launch connector was used to measure the fabricated design, and these connectors typically created the loss. A 1 inch long microstrip line test circuit on 8 mils RO4003 board provided by Southwest measured together with 2 of these connectors to measure the insertion loss of these connectors as shown in Figure 4.6, and results are shown in Figure 4.7. The reflection coefficients of the both ports have values better than -10 dB for the entire band. Moreover, the measured IL value at 28 GHz is 2.14 dB.

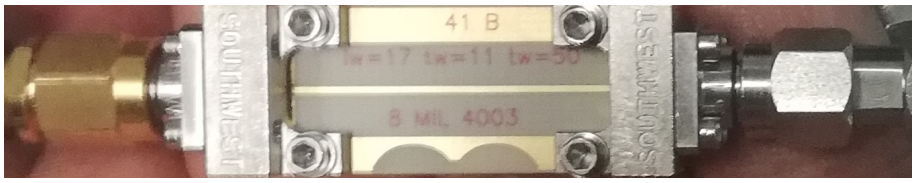

Figure 4.6 IL measurement setup of Southwest end launch connector.

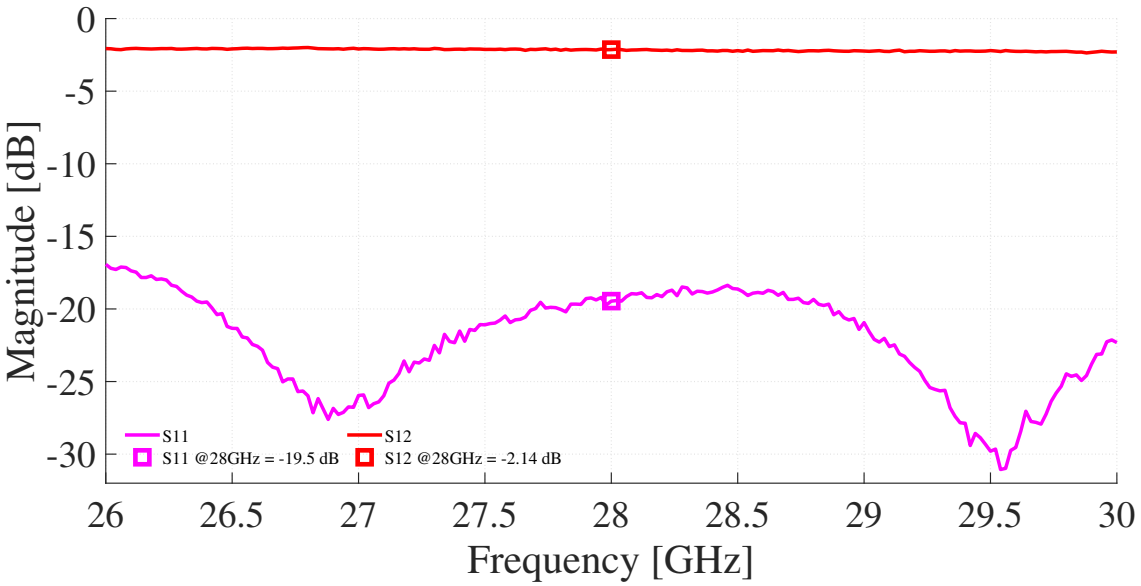

Figure 4.7 Measured scattering matrix of Southwest end launch connector.

4.2 Butler Matrix and 4×10 Rectangular Array

Designed antenna systems are fabricated using a low-cost PCB prototyping technique with an LPKF S63 milling machine at Sabanci University. The minimum achievable line width using this milling technique is 0.1 mm, with repeatability of ± 0.001 mm, which matches the minimum line width in the proposed design. Fabricated designs are shown in Figure 4.8, and the measurement setup is shown in Figure 4.9.

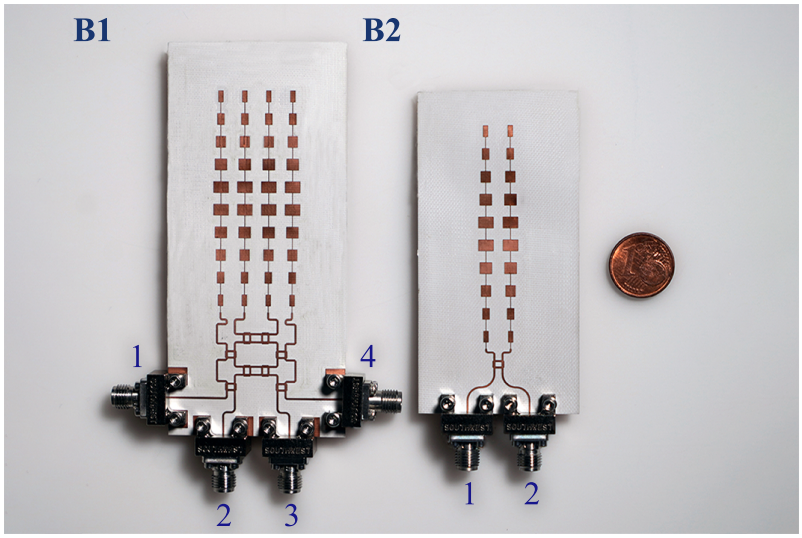

Figure 4.8 Fabricated 4×10 array antenna with BM and 2×10 array antenna with BLC together with corresponding port definition.

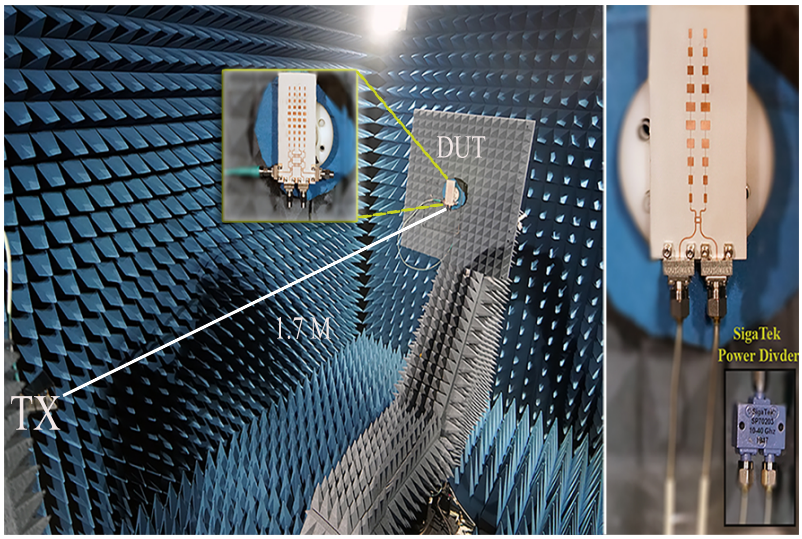

Figure 4.9 4×10 and 2×10 array antenna antenna with BM and BLC, fabrication and gain measurement.

The measured and simulated reflection coefficients of the 4×10 array antennas and BM are below with -10 dB between 26.5 to 29 GHz as shown in Figure 4.10. The

isolation value is below −10 dB between 26.5 to 28.5 GHz for all ports as shown in Figure 4.11. There is an improvement in the impedance bandwidth of the final design compared to the 1×10 alone, which occurs when BM is used as the BFN of the array antennas. Reflection coefficients values are minimum at 28.55 GHz for P1 and P4 with a value of −46 dB and −23 dB, respectively. The minimum reflection coefficient values of −30 dB occur at 28.33 GHz for P2 and P3. The minimum isolation values, with an isolation higher than 23 dB between all ports, occur for the frequency values near the 28 GHz.

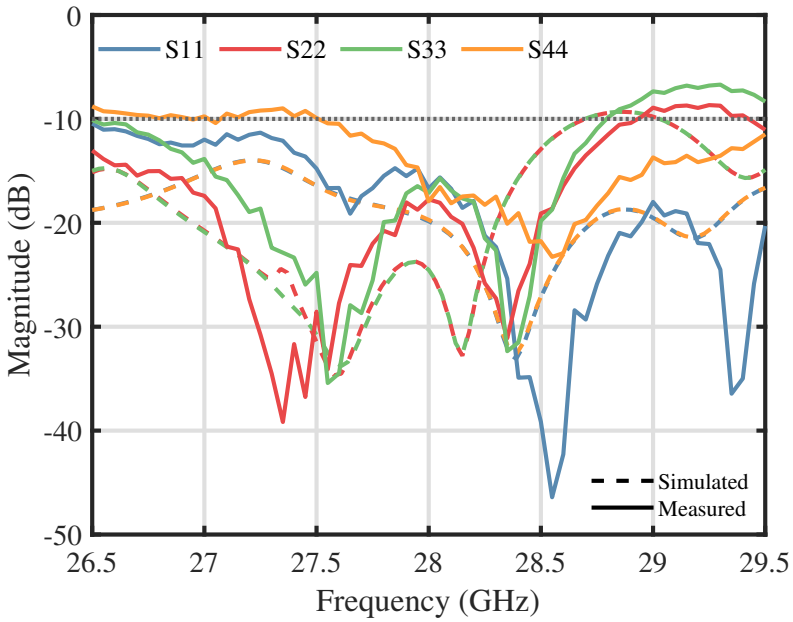

Figure 4.10 Measured and simulated reflection coefficients values of the 4×10 array antenna and BM.

Figure 4.12 illustrates the normalized measured and simulated gain value of 7 beams generated at 28 GHz. These beams are steered towards 10°, −44°, 38°, and,−10° once the individual ports P1, P2, P3, and P4 are excited. As a results, three additional beams are generated; a 26° beam, when P1 and P3 are excited, a 0° beam when P1 and P4 are excited, and a −29° beam when P2 and P4 are excited. In this manner, a −3-dB beamwidth of 112° is achieved between −70° to 50°. Figure 4.13 shows the gain value at different frequencies for the 4×10 array and BM structure which has a 1.62 GHz radiation bandwidth. The maximum average value of 12 dBi was achieved for all frequencies at 28.25 GHz, while the average gain over the frequency band of interest was 8.1 dBi.

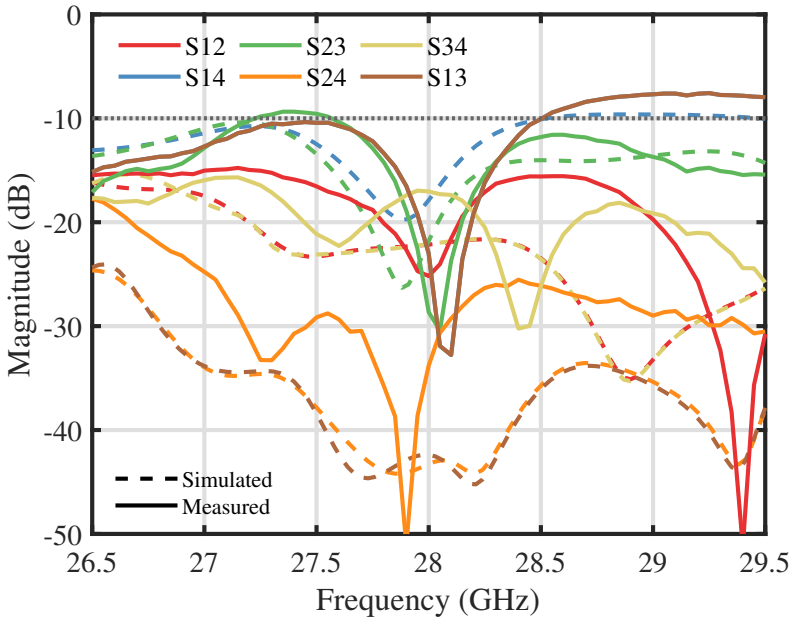

Figure 4.11 Measured and simulated scattering matrix value of the 4×10 array antenna and BM.

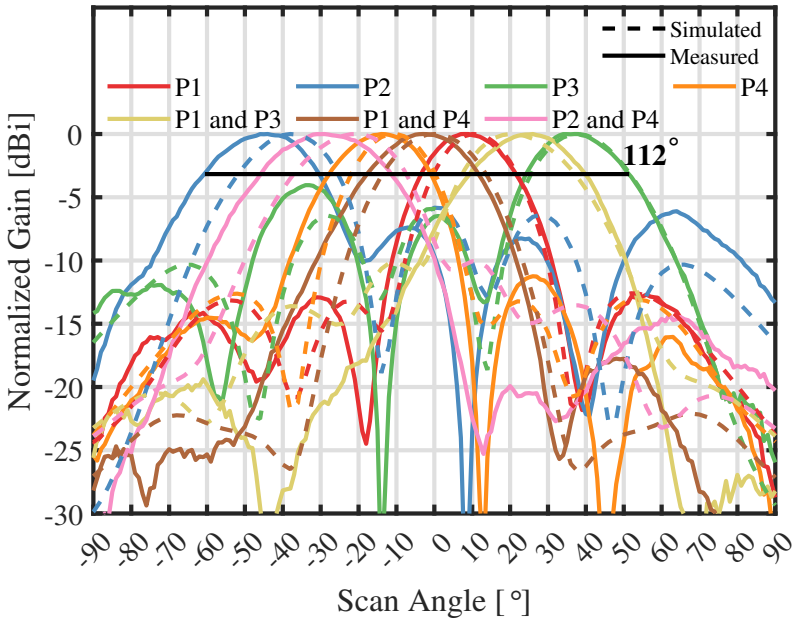

Figure 4.12 Measured and simulated normalized gains of three beams formed by the 4×10 array antenna with BM at 28 GHz and $\phi = 0°$-plane.

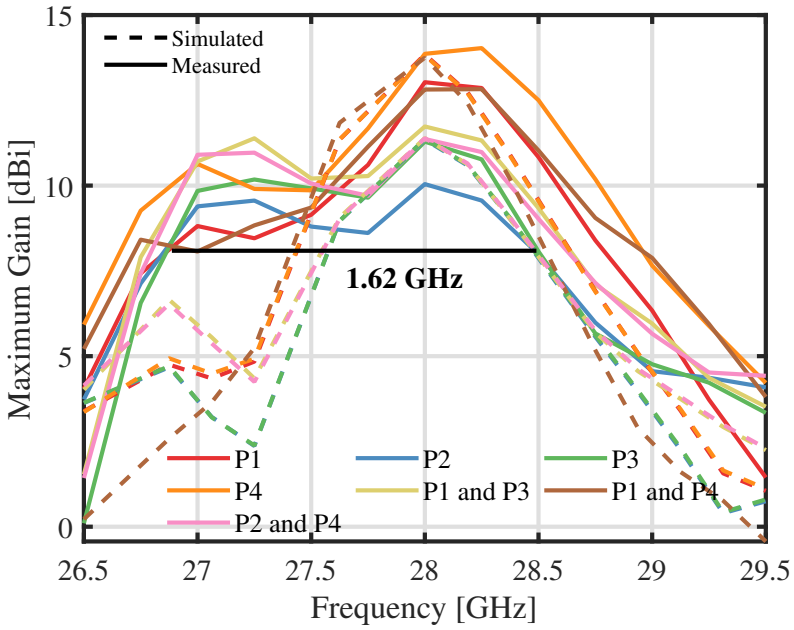

Figure 4.13 Simulated peak realized gain versus frequency of the 4×10 array antenna with BM.

4.3 Branch Line Coupler and 2×10 Rectangular Array

Figure 4.14 shows the measured and simulated reflection and isolation values of the BLC with 2×10 array system. The measured and simulated reflection coefficients are below; -10 dB for the 26.5 to 29.5 GHz band for both ports of the system. A minimum value of -40 dB at 29.5 GHz for P1 and -35 dB at 29.15 GHz for P2 was measured as shown in Figure 4.14.

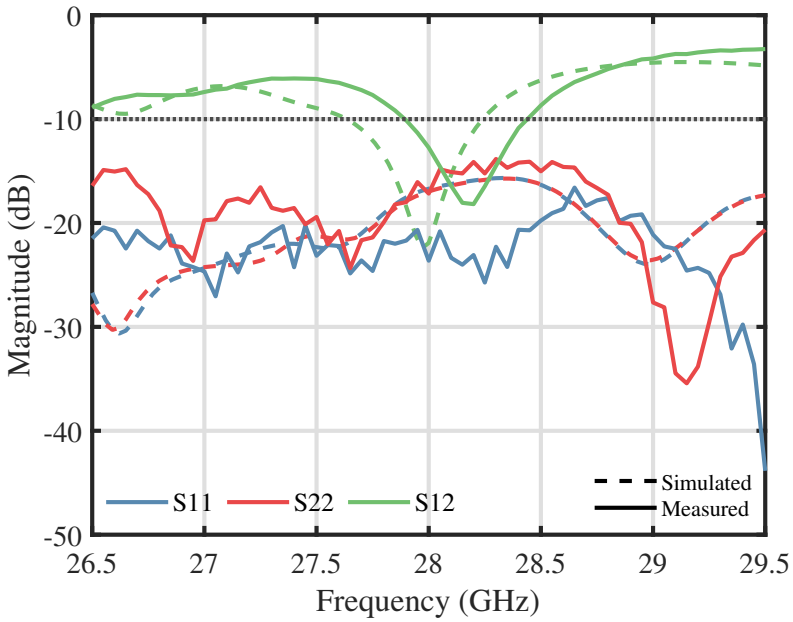

Figure 4.14 Measured and simulated reflection coefficients values of the 2×10 array antenna and BLC.

While the isolation bandwidth is more narrow, since a 3-dB coupler BFN was used prior to the 2×10 array, measured isolation values are experiencing a minor shift with respect to the frequency as shown in Figure 4.14. That being said, the measured isolation values follow the same trend as the simulation and this shift in the center frequency is negligible. The mentioned differences between simulation and measurement might be due to fabrication or measurement errors; such as a misalignment of the connector pin. Furthermore, a minimum isolation value of -18 dB at 28.2 GHz and isolation values better than -10 dB for 27.9 GHz to 28.45 GHz were achieved.

Figure 4.15 shows the measured and simulated normalized gain values of 3 generated beams by BLC and a 2×10 array at 28 GHz, and a 3-dB beamwidth of 90° achieved between $-45°$ to 45°. P1 and P2 excite the main beams steered towards $-20°$, and 20°, respectively and, exciting P1 and P2 simultaneously generates a beam at 0°. With the same excitation order, a measured, maximum realized gain value of 11.7

dBi, 11.7 dBi, 12.5 dBi was achieved at 28 GHz. Moreover, the measured versus simulated antenna gains are approximately identical once compensated for the loss of the additional cables and the power divider.

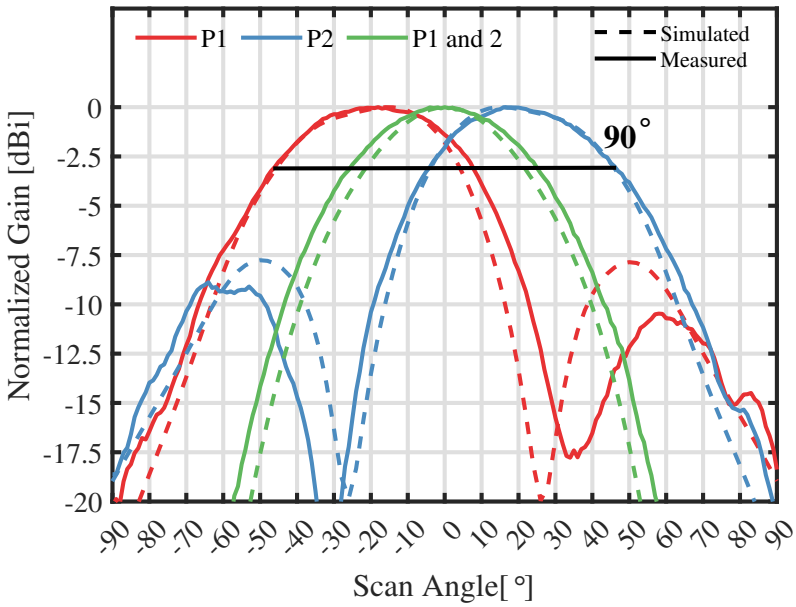

Figure 4.15 Measured and simulated normalized gains of the three beams formed by the 2×10 array antenna with BLC at 28 GHz and $\phi = 0°$-plane.

In Figure 4.16, simulated and measured maximum gain values are obtained between 26.5 GHz and 29.5 GHz, and a radiation bandwidth of 1.85 GHz is achieved with a gain value higher than 8 dBi. The average gain value over the band of interest is 7.4 dBi. The maximum measured gain values of 11.4 dBi and 11.6 dBi were achieved at 28.25 GHz by exciting P1 only and P2 only, respectively, where excitation of P1 and P2 simultaneously generate a maximum gain of 13.4 dBi.

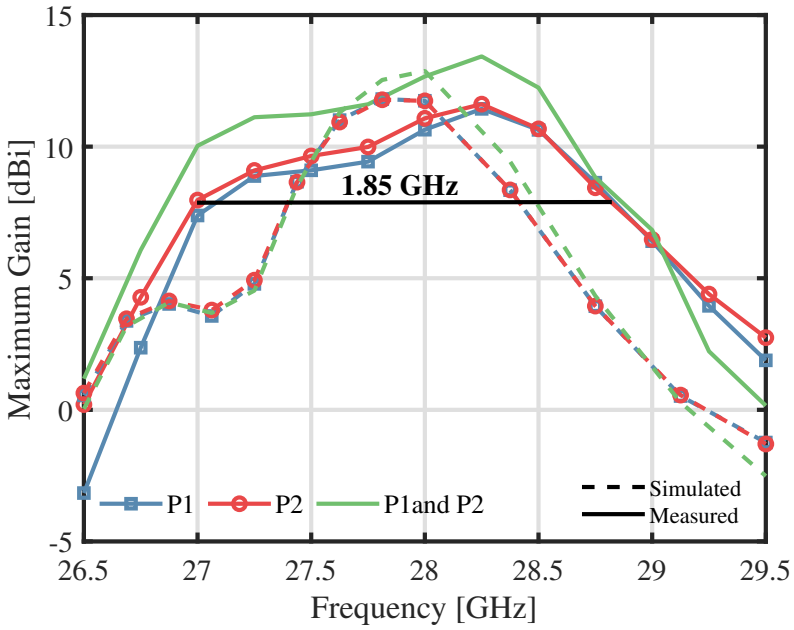

Figure 4.16 Measured and simulated maximum gains of the 2×10 array antenna with BLC versus frequency.

4.4 Branch Line Coupler and 2×10 Elliptical Array

The final design for this elements was fabricated with LPKF S63 in the Sabanci University Collaboration Space facility as well. The minimum line width achievable with the LPKF S63 milling technique is 0.1 mm, satisfying our minimum design requirements. The fabricated 2×10 PAA with BLC is shown in Figure 4.17. The Southwest end launch connector was used to measure the fabricated design. The P1&P2 ports were excited with a SigaTek SP70203 power divider to form the M beam. An Agilent PNA 5245A vector network analyzer (VNA) was used to measure the scattering matrix of the design.

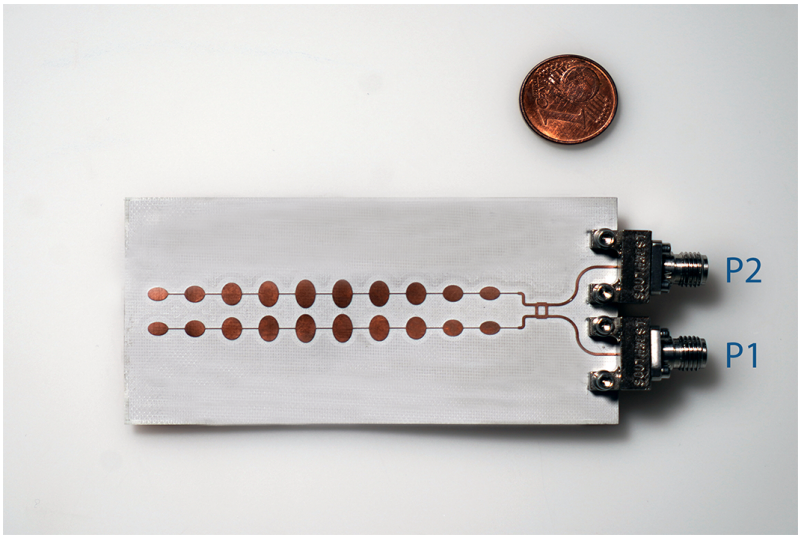

Figure 4.17 Fabricated 2×10 PAA with BLC

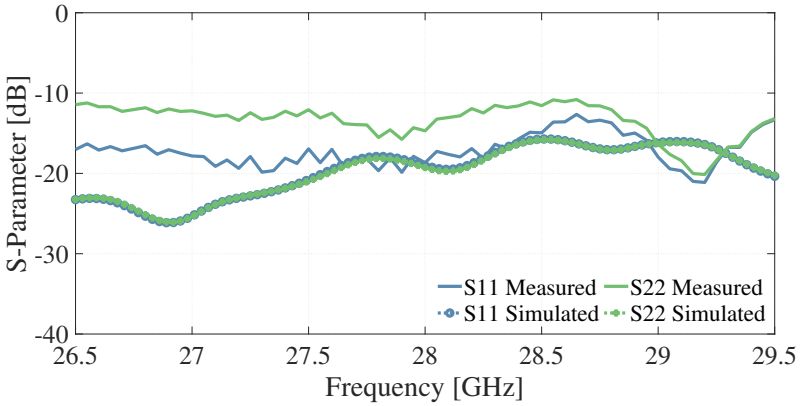

Figure 4.18 Measured and simulated S-parameters for 2×10 PAA with BLC.

Next, the anechoic chamber facility of Sabanci University Nano Technology Center was used to measure the gain characteristic of the fabricated design. Inside the chamber, the distance between the device under test (DUT) and transmitter antenna

(TX) was 1.7 meters. In Fig. 4.18 the measured and simulated S-parameters values of 2×10 PAA with BLC are given.

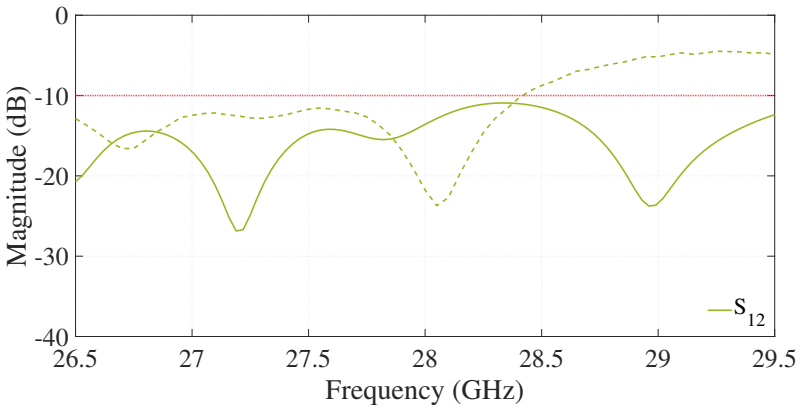

Figure 4.19 Measured and simulated isolation for 2×10 PAA with BLC.

The reflection coefficients of both ports were below -10 dB and isolation between the two ports was higher than 10 dB over the band as shown in Figure 4.19. This improvement in the overall impedance bandwidth is because of adding BLC to PAA.

The simulated results do not include the losses of the power divider and end launch connectors used in the measurement. For this reason, after calculating the insertion loss of connectors and the power divider, these needed to be calibrated. Measured and simulated gain values were normalized with respect to their maximums and plotted on top of each other in Fig. 4.20. The main lobe levels and directions were matched with those in the simulation, with a beam offset of ± 2 degrees and beam value error of less than 0.5 dBi.

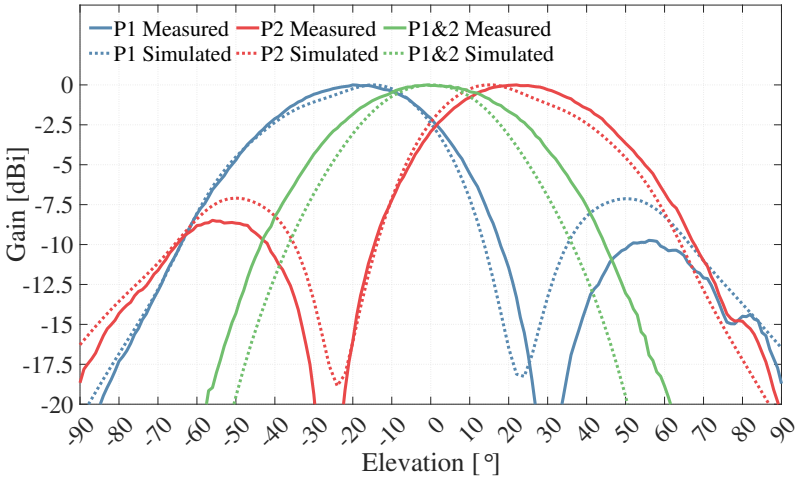

Figure 4.20 Measured and simulated normalized gains of three beams formed by 2×10 PAA with BLC.

The minor differences in the simulated and fabricated results can likely be attributed to the resolution quality of the fabrication or the indeterminable imperfection of the

measurement in the anechoic chamber. For instance, the imperfection created by the quality of the end launch connectors and/or cables, or misplacement of the connector pin at the excitation point.

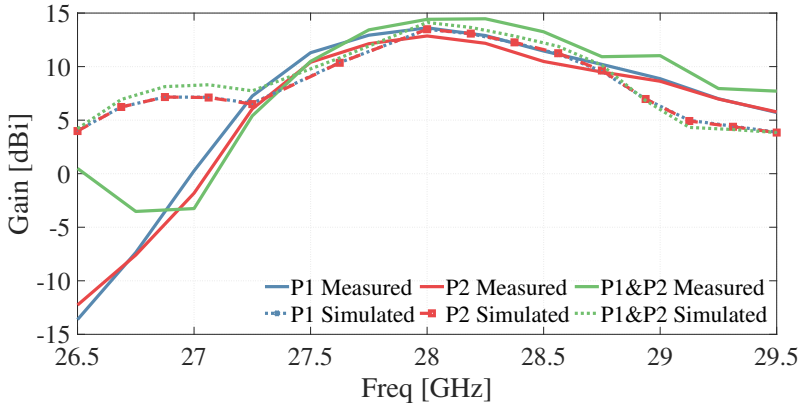

Figure 4.21 Maximum simulated and measured 2×10 PAA with BLC realized gain versus frequency at $\phi = 0$.

In Figure 4.21 un-normalized gain values of the simulated and measured beams are shown over the band for $\phi = 0$, 1.5 bandwidth achieved with more than 10 dBi gain value while for more than 5 dBi gain a 2.3 GHz bandwidth achieved. As expected, the maximum gain values occurred at around 28 GHz, and the gain value followed the same trends as the simulated peak realized gain value. However, the lower value of the measured gain as compared to the simulated gain is at least partly due to the fact that the beam shifted in the ϕ-direction as frequency changed. The antenna's efficiency is simulated in HFSS, and 40% efficiency is obtained at 28 GHz.

Chapter 5

CONCLUSION AND FUTURE WORKS

Unique feeding and a strategic array placement configuration resulted in the increased angular coverage of a conventional Butler matrix and branch line coupler fed Chebyshev tapered series of arrays. The conventional Butler matrix can generate 4 beams. However, we could generate 7 beams from a Butler matrix with simultaneous port feeds. Similarly, we generated 3 beams from a 2 beam generation capable branch-line coupler. A 4×10 array is fed with a Butler matrix and placed on the broadside of a phone, and two 2×10 arrays, fed with BLC, are placed on the two narrow sides of the phone generating 13 beams from 8 ports. For the 4×10 array, the impedance bandwidth was 3 GHz, and the gain bandwidth was 1.62 GHz with beams with peak gain values varying between 11.2 to 14.1 dBi. For the 2×10 array, the 10 dB impedance bandwidth was 3 GHz, and the gain bandwidth was 1.85 GHz. Combining a 4×10 and two 2×10 array cover ± 138 of angular space. The proposed design was fabricated on RO4003, using a low-cost PCB fabrication technique. The final design used a two-layer, low-cost, compact microstrip topology with dimensions of $90 \times 45 \times 11$ mm^3 and a comparable gain value as to the SIW designs. A Chebeysheved tapered elliptic microstrip PAA with its beamforming network was designed and optimized to operate at the 28 GHz 5G band on the RO4003 board for cellular phone applications. The final design can generate three beams with a realized gain of above 10 dBi for -45° to 45° coverage.

The same method can be used for other types such as 8×8 BM to create more beams, and it will be possible to reduce the number of the ports using the switching network prior to the BM to decrease the number of the port in the final system.

The elliptic element improves the overall bandwidth performance of the design from

26.5 GHz to 29.5 GHz compared to rectangular series fed arrays. The slot-loaded elliptical elements significantly improved the antenna array's radiation performance in the band of interest. With this element achieving a broadband flat gain performance become possible. The slot-loaded design will be measured after fabrication.

BIBLIOGRAPHY

[1] H. Yu, H. Lee, and H. Jeon, "What is 5G? emerging 5G mobile services and network requirements," *Sustainability (Switzerland)*, vol. 9, 10 2017.

[2] 3rd Generation Partnership Project (3GPP), "22.891. feasibility study on new services and markets technology enablers.," 2016.

[3] J. Wang, A. Jin, D. Shi, L. Wang, H. Shen, D. Wu, L. Hu, L. Gu, L. Lu, Y. Chen, J. Wang, Y. Saito, A. Benjebbour, and Y. Kishiyama, "Spectral efficiency improvement with 5G technologies: Results from field tests," *IEEE Journal on Selected Areas in Communications*, vol. 35, pp. 1867–1875, 8 2017.

[4] 3rd Generation Partnership Project (3GPP), "Technical specification group radio access network; NR; User Equipment (UE) radio transmission and reception release 17," 2021.

[5] S. Rajagopal, S. Abu-Surra, Z. Pi, and F. Khan, "Antenna array design for multi-Gbps mmwave mobile broadband communication," in *2011 IEEE Global Telecommunications Conference - GLOBECOM 2011*, pp. 1–6, 2011.

[6] R. Chopra and G. Kumar, "Series-fed binomial microstrip arrays for extremely low sidelobe level," *IEEE Transactions on Antennas and Propagation*, vol. 67, pp. 4275–4279, 6 2019.

[7] C. Deng, D. Liu, B. Yektakhah, and K. Sarabandi, "Series-fed beam-steerable millimeter-wave antenna design with wide spatial coverage for 5G mobile terminals," *IEEE Transactions on Antennas and Propagation*, vol. 68, pp. 3366–3376, 5 2020.

[8] Y. Q. Guo, Y. M. Pan, and S. Y. Zheng, "Design of series-fed, single-layer, and wideband millimeter-wave microstrip arrays," *IEEE Transactions on Antennas and Propagation*, vol. 68, pp. 7017–7026, 10 2020.

[9] D. Ehyaie and A. Mortazawi, "A new approach to design low cost, low complexity phased arrays," in *2010 IEEE MTT-S International Microwave Symposium*, pp. 1270–1273, 2010.

[10] H. Mirzaei and G. V. Eleftheriades, "Eliminating beam-squinting in wideband linear series-fed antenna arrays using feed networks constructed by slow-wave transmission lines," *IEEE Antennas and Wireless Propagation Letters*, vol. 15, pp. 798–801, 2016.

[11] S. Keser and M. Mojahedi, "Removal of beam squint in series fed array antennas using abnormal group delay phase shifters," in *2010 IEEE Antennas and Propagation Society International Symposium*, pp. 1–4, 2010.

[12] J. Li, C. He, H. Fan, and R. Jin, "Gain-equalized multibeam antenna fed by a compact dual-layer Rotman lens at Ka-band," *IEEE Transactions on Antennas and Propagation*, pp. 1–1, 9 2021.

[13] M. Heino, C. Icheln, J. Haarla, and K. Haneda, "PCB-based design of a beam-steerable array with high-gain antennas and a Rotman lens at 28 GHz," *IEEE Antennas and Wireless Propagation Letters*, vol. 19, pp. 1754–1758, 10 2020.

[14] S. Trinh-Van, J. M. Lee, Y. Yang, K. Y. Lee, and K. C. Hwang, "A sidelobe-reduced, four-beam array antenna fed by a modified 4×4 Butler matrix for 5G applications," *IEEE Transactions on Antennas and Propagation*, vol. 67, pp. 4528–4536, 7 2019.

[15] C. Qin, F. C. Chen, and K. R. Xiang, "A 5×8 Butler matrix based on substrate integrated waveguide technology for millimeter-wave multibeam application," *IEEE Antennas and Wireless Propagation Letters*, vol. 20, pp. 1292–1296, 7 2021.

[16] H. Ren, H. Zhang, Y. Jin, Y. Gu, and B. Arigong, "A novel 2-D 3×3 Nolen matrix for 2-D beamforming applications," *IEEE Transactions on Microwave Theory and Techniques*, vol. 67, no. 11, pp. 4622–4631, 2019.

[17] F. Abdul Ghani, A. M. A. Najafabadi, H. Saleh, M. Kaya Yapici, and I. Tekin, "A 28 GHz 2×2 antenna array with 10 beams using passive SPDT switch beamforming network," *Sensors*, vol. 21, no. 21, 2021.

[18] S. P. Yan, M. H. Zhao, Y. L. Ban, J. W. Lian, and Z. Nie, "Dual-layer SIW multibeam pillbox antenna with reduced sidelobe level," *IEEE Antennas and Wireless Propagation Letters*, vol. 18, pp. 541–545, 3 2019.

[19] C. D. Paola, K. Zhao, S. Zhang, and G. F. Pedersen, "SIW multibeam antenna array at 30 GHz for 5G mobile devices," *IEEE Access*, vol. 7, pp. 73157–73164, 2019.

[20] Q. Sun, Y. L. Ban, J. W. Lian, Y. Liu, and Z. Nie, "Millimeter-wave multibeam antenna based on folded C-type SIW," *IEEE Transactions on Antennas and Propagation*, vol. 68, pp. 3465–3476, 5 2020.

[21] M. Khalily, R. Tafazolli, P. Xiao, and A. A. Kishk, "Broadband mm-wave microstrip array antenna with improved radiation characteristics for different 5G applications," *IEEE Transactions on Antennas and Propagation*, vol. 66, pp. 4641–4647, 9 2018.

[22] H. A. Diawuo and Y. B. Jung, "Broadband proximity-coupled microstrip planar antenna array for 5G cellular applications," *IEEE Antennas and Wireless Propagation Letters*, vol. 17, pp. 1286–1290, 7 2018.

[23] R. Chopra and G. Kumar, "Series-fed binomial microstrip arrays for extremely low sidelobe level," *IEEE Transactions on Antennas and Propagation*, vol. 67, pp. 4275–4279, 6 2019.

[24] E. V. Anjos, D. M. Schreurs, G. A. Vandenbosch, and M. Geurts, "A 15-43.5 GHz switched-bit phase shifter for 5G mobile handsets," vol. 2019-December, pp. 165–167, Institute of Electrical and Electronics Engineers Inc., 12 2019.

[25] R. B. Yishay and D. Elad, "Low loss 28 GHz digital phase shifter for 5G phased array transceivers," 2018.

[26] M. Salarrahimi, E. V. P. D. Anjos, P. Taghikhani, V. Volski, C. Fager, D. M. Schreurs, G. A. Vandenbosch, and M. Geurts, "A cost-efficient 28 GHz integrated antenna array with full impedance matrix characterization for 5G NR," *IEEE Antennas and Wireless Propagation Letters*, vol. 19, pp. 666–670, 4 2020.

[27] S. Zhang, I. Syrytsin, and G. F. Pedersen, "Compact beam-steerable antenna array with two passive parasitic elements for 5G mobile terminals at 28 GHz," *IEEE Transactions on Antennas and Propagation*, vol. 66, pp. 5193–5203, 10 2018.

[28] E. Garcia-Marin, J. L. Masa-Campos, and P. Sanchez-Olivares, "Planar array topologies for 5G communications in Ku-band [wireless corner]," *IEEE Antennas and Propagation Magazine*, vol. 61, no. 2, pp. 112–133, 2019.

[29] A. M. A. Najafabadi, F. A. Ghani, and I. Tekin, "Low-cost multibeam millimeter-wave array antennas for 5G mobile applications," *IEEE Transactions on Vehicular Technology*. Manuscript submitted.

[30] A. M. A. Najafabadi, F. A. Ghani, and I. Tekin, "A 28 GHz beam steerable elliptic microstrip array antenna for 5G applications," in *2022 16th European Conference on Antennas and Propagation (EuCAP)*, pp. 1–4, 2022.

[31] C. A. Balanis, *Antenna Theory: Analysis and Design, 4th ed.* Wiley, 2015.

[32] W. L. Stutzman and G. A. Thiele, *Antenna Theory and Design, 2nd Edition*. Wiley, 1997.

[33] R. J. Mailloux, *Phased Array Antenna Handbook, 3rd ed.* Artech, 2018.

[34] H. J. Visser, *Array and Phased Array Antenna Basics*. Wiley, 2005.

[35] R. E. Collin, *Antennas and Radiowave Propogation*. McGraw-Hill, 1985.

[36] "5G antenna white paper new 5G, new antenna," *HUWAEI*.

[37] Y. J. Guo and R. W. Ziolkowski, *Advanced Antenna Array Engineering for 6G and Beyond Wireless Communications*. Wiley, 2022.

[38] W. Hong, Z. H. Jiang, C. Yu, J. Zhou, P. Chen, Z. Yu, H. Zhang, B. Yang, X. Pang, M. Jiang, Y. Cheng, M. K. T. Al-Nuaimi, Y. Zhang, J. Chen, and S. He, "Multibeam antenna technologies for 5G wireless communications," *IEEE Transactions on Antennas and Propagation*, vol. 65, no. 12, pp. 6231–6249, 2017.

[39] B. Sadhu, Y. Tousi, J. Hallin, S. Sahl, S. Reynolds, Renström, K. Sjögren, O. Haapalahti, N. Mazor, B. Bokinge, G. Weibull, H. Bengtsson, A. Carlinger, E. Westesson, J.-E. Thillberg, L. Rexberg, M. Yeck, X. Gu, D. Friedman, and A. Valdes-Garcia, "7.2 a 28Ghz 32-element phased-array transceiver IC with concurrent dual polarized beams and 1.4 degree beam-steering resolution for 5G communication," in *2017 IEEE International Solid-State Circuits Conference (ISSCC)*, pp. 128–129, 2017.

[40] G.-S. Shin, J.-S. Kim, H.-M. Oh, S. Choi, C. W. Byeon, J. H. Son, J. H. Lee, and C.-Y. Kim, "Low insertion loss, compact 4-bit phase shifter in 65 nm CMOS for 5G applications," *IEEE Microwave and Wireless Components Letters*, vol. 26, no. 1, pp. 37–39, 2016.

[41] D. M. Pozar, *Microwave Engineering*. Wiley, 2012.

[42] N. Kou, Z. S. Yu, Ding, and Z. Zhang, "One-dimensional beam scanning transmitarray lens antenna fed by microstrip linear array," *IEEE Access*, vol. 7, pp. 90731–90740, 2019.

[43] S. Kim, S. Yoon, Y. Lee, and H. Shin, "A miniaturized butler matrix based switched beamforming antenna system in a two-layer hybrid stackup substrate for 5G applications," *Electronics*, vol. 8, p. 1232, 2019.

[44] J.-W. Lian, Y.-L. Ban, J.-Q. Zhu, J. Guo, and Z. Chen, "Planar 2-D scanning SIW multibeam array with low sidelobe level for millimeter-wave applications," *IEEE Transactions on Antennas and Propagation*, vol. 67, no. 7, pp. 4570–4578, 2019.

[45] Y. Cao, K.-S. Chin, W. Che, W. Yang, and E. S. Li, "A compact 38 GHz multibeam antenna array with multifolded Butler matrix for 5G applications," *IEEE Antennas and Wireless Propagation Letters*, vol. 16, pp. 2996–2999, 2017.

[46] Y. Liu, O. Bshara, I. Tekin, and K. R. Dandekar, "A 4 by 10 series 60 GHz microstrip array antenna fed by Butler matrix for 5G applications," pp. 1–4, Institute of Electrical and Electronics Engineers Inc., 5 2018.

[47] M. Ansari, H. Zhu, N. Shariati, and Y. J. Guo, "Compact planar beamforming array with endfire radiating elements for 5G applications," *IEEE Transactions on Antennas and Propagation*, vol. 67, no. 11, pp. 6859–6869, 2019.